


Article

Numerical Study on Fire Suppression by Water Mist in Aircraft Cargo Compartments: Effects of Spray Pattern, Droplet Size, and Nozzle Layout

Pei Zhu ^{1,*}, Ziheng Xu ¹, Jiangao Zhang ¹, Quan Shao ¹, Weiwang Chen ² and Hongzhou Ai ³

¹ College of Civil Aviation, Nanjing University of Aeronautics and Astronautics, Nanjing 210016, China; xuziheng@nuaa.edu.cn (Z.X.); zhang.jiangao@nuaa.edu.cn (J.Z.); shaoquan@nuaa.edu.cn (Q.S.)

² Key Laboratory of Civil Aviation Thermal Disaster Prevention and Emergency, Civil Aviation University of China, Tianjin 300300, China; ww_chen@cauc.edu.cn

³ Civil Aircraft Fire Science and Safety Engineering Key Laboratory of Sichuan Province, Civil Aviation Flight University of China, Guanghan 618307, China; aihongzhou@cafuc.edu.cn

* Correspondence: zpei@nuaa.edu.cn

Abstract: Aircraft cargo compartment fires are one of the main threats to the safety of civil aircraft. In this study, a series of numerical simulations on the fire suppression performance of water mist in cargo compartments was carried out to examine the effects of the spray pattern, droplet size, and nozzle layout. The fire dynamics simulator (FDS) code was used to construct a fire suppression scenario in a full-scale aircraft cargo compartment. The results show that the extinguishment time of a corner fire was longer compared with center and sidewall fires due to the relatively larger distance from the nozzle and, therefore, a lower effective number of droplets reaching the flame area. Solid and hollow spray patterns showed significant differences in the spray coverage area. For a fixed flow rate, the hollow spray showed better fire suppression performance than solid spray. When the droplet size varied from 50 to 400 μm , the fire extinguishment time first increased and then decreased, corresponding to the dominant mechanism of the smothering effect of small droplets and the cooling effect of large droplets. In addition, the nozzle layout affected the water coverage on the ground of the cargo compartment. With an increase in nozzle number, the water mist flux was more evenly distributed and the fire extinguishment effect also increased.

Keywords: aircraft cargo compartment; fire suppression; CFD modeling; water mist; spray pattern; nozzle layout



Citation: Zhu, P.; Xu, Z.; Zhang, J.; Shao, Q.; Chen, W.; Ai, H. Numerical Study on Fire Suppression by Water Mist in Aircraft Cargo Compartments: Effects of Spray Pattern, Droplet Size, and Nozzle Layout. *Fire* **2024**, *7*, 481. <https://doi.org/10.3390/fire7120481>

Academic Editors: Ruichao Wei, Shengfeng Luo and Xuehui Wang

Received: 11 November 2024

Revised: 8 December 2024

Accepted: 11 December 2024

Published: 17 December 2024



Copyright: © 2024 by the authors. Licensee MDPI, Basel, Switzerland. This article is an open access article distributed under the terms and conditions of the Creative Commons Attribution (CC BY) license (<https://creativecommons.org/licenses/by/4.0/>).

1. Introduction

Air transport is an important mode of transportation. However, in-flight fires can lead to catastrophic disasters, as evacuation becomes impossible, especially for Class C cargo compartment fires. This poses a high risk on board due to the presence of large amounts of combustible materials, ignited by the overheating of heating pipes, short circuits of wires, spontaneous combustion, static electricity, lithium battery explosions, and so on. In addition, aircraft cargo compartments are usually regarded as confined spaces, with low temperatures, low in-flight pressure, and limited ventilation, which will further aggravate the damage resulting from fires. According to the International Civil Aviation Organization (ICAO), ten serious aircraft fire incidents occurred in the decade from 2011 to 2021, resulting in serious aircraft damage and fatalities [1]. Therefore, the study of the combustion of materials in aircraft and the effects of combustion on the human body and airframe structures is part of greater efforts to improve the safety of air transport.

When a fire occurs and is detected, extinguishing it in the cargo compartment of an aircraft quickly and efficiently is an important means of reducing the resulting damages. For cargo compartments, fixed total-flood fire extinguishment or suppression systems

are used, i.e., an extinguishing agent is discharged into an enclosed space to achieve a concentration sufficient to extinguish or suppress an existing fire. Halon 1301 is popular as a suppression agent due to its favorable properties in suppressing fire, namely, its electric non-conductivity, rapid dissipation without residue, and relatively safe utilization [2]. However, the emission of halon can cause significant damage to the ozone layer, and its production was banned in 1994 following the Montreal Protocol international agreement [3]. The European Aviation Safety Agency set the halon commission end-date at 2040 for fixed fire suppression systems [4]. Now, all efforts are focused on finding a replacement that yields the same results as halon for fire control in enclosed spaces. These replacement agents must have low ozone depletion potential (ODP) and toxicity and be residue-free and easy to clean up, with a low global warming potential (GWP) and a low risk of use (relative to Halon 1301 systems), among others [5]. Meanwhile, any candidate agent being considered is required to undergo rigorous testing in accordance with the minimum performance standard (MPS) [6] developed by the International Systems Fire Protection Working Group, which includes four fire scenarios—a bulk-load fire test, a containerized-load fire test, a surface burning test, and an aerosol can explosion test. The “Options Report” of the Federal Aviation Administration (FAA) lists commercialized total-flooding agents of halon replacements [3]. Water mist is one promising fire extinguishing agent, due to its effectiveness, low-cost, and cleanness. The use of water mist as a halon alternative in aircraft cargo compartments has been documented and studied by the Federal Aviation Administration [5]. In the current study, a surface burning fire scenario involving a square pool of fire with a length of 60.9 cm and Jet-A fuel was adopted to validate and analyze the fire suppression performance of water mist with specific spray characteristics in aircraft cargo compartments.

There are five mechanisms associated with the extinguishment of class B (flammable liquid) fires by water mist [7,8], namely, gas-phase cooling, oxygen displacement and flammable vapor dilution, the wetting and cooling of the fuel surface, radiation attenuation, and kinetic effects. Recently, numerical simulations and experimental research progress regarding the efficacy of water mist in suppressing hydrocarbon fires in enclosures were systematically reviewed by Moinuddin et al. [9]. For example, many experimental efforts have focused on the effects of a confined space [10] on water mist performance, as well as nozzle geometry [11,12], spray characteristics [13], the presence of objects shielding the fire [14], and other configurations. However, full-scale experiments in such compartments are time-consuming and expensive, so computational fluid dynamics (CFD)-based fire models can be considered as an alternative method to predict the physics of fire and water mist interactions in enclosed spaces [10]. As such, they are increasingly used in all aspects of fire safety engineering. In addition, CFD simulations can also help to visualize flow patterns, which could easily indicate critical operating variables and provide guidance for experimental setups. In this paper, the numerical simulation method was adopted due to the limitations of full-scale aircraft cargo compartment fire experiments. Currently, CFD simulations of issues related to fire suppression scenarios are widely conducted utilizing a fire dynamics simulator (FDS), with a few instances employing FireFOAM and a scant number employing FLUENT and other codes [10,15–34]. In order to accurately predict the conditions required for extinguishment, the combustion chemistry, thermodynamics, and fluid dynamics need to be modelled in detail. In addition, the results of the numerical model need to be validated against experimental test results.

For the simulation of pool fire suppression by water mist systems, numerical models of pool fires, water spray, and flame extinction need to be considered. The research progress of pool fire dynamics was recently reviewed in [15], including the burning rate, flame characteristics, radiation, and soot formation through experimental and numerical simulation methods. Baglatzis et al. [16] used FireFoam and FDS numerical codes to study the characteristics of pool fires; the results were compared with experimental data to verify their credibility. Cavazzuti et al. [17] used FireFoam to simulate a pool fire in a large under-ventilated environment; the results showed good agreement with experimental data.

The above studies only focused on a pure fuel (n-heptane) pool fire, but Jet-A aviation kerosene is used presently, which is a mixture of various hydrocarbons [18]. However, the modelling of oxidation and combustion reactions with a detailed chemical kinetic model, given the large number of compounds in aviation fuels, is a significant challenge. A surrogate fuel with either a single component or mixtures with a simplified chemical reaction mechanism has been adopted by most researchers [18–21]. For example, Alekseev et al. [18] investigated the Laminar burning velocities of an n-decane and binary surrogate mixture. Yan et al. [19] proposed a simplified chemical reaction mechanism for binary mixtures composed of n-decane ($C_{10}H_{22}$) and n-propylbenzene (C_9H_{12}) as a surrogate fuel for Jet-A. Humer et al. [20] just used surrogate fuel with an average molecular formula of $C_{12}H_{23}$ to simulate the laminar non-premixed flows of gas Jet-A. Similarly, fuel with an average molecular formula of $C_{11.4}H_{21.7}$ was used in this paper. But these studies only focused on laminar combustion or an internal aero-engine combustion chamber; few have considered pool fire simulations with Jet-A. Recently, Gianmaria et al. [21] proposed a reduced kinetic mechanism consisting of 14 reactions, which was implemented in an FDS model to simulate a pool fire with aviation fuel. Experimental data of heating flux may be well reproduced by either the detailed kinetic mechanism or a simple chemistry model. But the results indicated that aviation fuel soot formation was considerably affected by local conditions, e.g., oxygen content and temperature, and complex models were required to account for these parameters. In the current study, the introduction of water spray in a cargo compartment was found to lead to a more complicated conditions, which would bring huge challenges to the calculation of the kinetic mechanism. This would also require substantial computational resources and bring about theoretical difficulties. Therefore, the simple chemistry model in FDS may be more suitable for dealing with complex fire extinguishing scenarios.

For fire protection or suppression using water spray, a lot of research [22–35] has been done using experimental and numerical simulation methods. For the use of FDS, Zhu et al. [22] conducted a series of experimental and numerical tests on the attenuation of thermal radiation from large-scale pool fires using a water mist curtain, where the HRR was prescribed with estimated fire growth periods. Jenft et al. [23] treated liquid fuel as a solid fuel and used the Arrhenius relationship to model pyrolysis instead of the evaporation model in FDS to simulate a pool fire. The simulated configurations of the particle injection rate and mist flux distribution by Beji et al. [24], droplet size by Liu et al. [25], ventilation conditions by Lee [26], multiple pool fires suppression [27], fire suppression time by Ha et al. [28], a physical and sensitivity analysis by Robinet et al. [29], droplet impact and coverage area by De Cachinho Cordeiro et al. [30], and nozzle characteristics by Gui et al. [31] for fire suppression via water mist system have been conducted, and relatively accurate results in engineering applications were obtained. In the above studies, most cases treated pool fire growth using a prescribed HRR method, with peak HRR based on the theoretical burning rate, namely, the standard t-squared model or tan h model. Hypotheses and simplifications regarding FDS models will be introduced in Section 2.1. In addition, Vilfayeau et al. [32] validated flame cooling effectiveness by water mist using FireFoam and found that maximum suppression occurred when mist droplets were entrained into the flame base region. Liu et al. [33] proposed a novel stochastic approach to study water droplet/flame interactions using ANSYS Fluent 19.2; the results indicated that tracing the transient movement and evaporation process of water droplets could be used to effectively study the heat transfer efficiency of water-based fire suppression systems.

The above studies mainly focused on fire scenarios in buildings or industrial facilities on the ground, but fires in aircraft cargo compartments show significant differences due to the confined space, complex ambient conditions, random ignition locations, strict fire extinguishing requirements, and limited fire control resources [34], especially for the cruising phase. It should be noted that the main objective of the water mist fire suppression system in a cargo compartment is to provide a period of protection, allowing the airplane to land safely. A series of fire extinguishing experiments by water spray or mist in full-scale

cargo compartments was conducted by the Federal Aviation Administration [35,36], who concluded that a hybrid water mist and nitrogen system can meet the minimum performance standards, and water consumption can be reduced by more than 50% compared with single-fluid systems. Payri et al. [37] studied the dispersion of water and novect1230 through a real-sized extinguisher nozzle under realistic aircraft cargo cabin conditions. The numerical simulation method has been widely used and validated for the assessment of aircraft cargo compartment fire suppression systems [38,39]. Zhu et al. [40,41] studied synergetic fire suppression with nitrogen/water-mist in a full-scale aircraft cargo compartment using experimental measurements and numerical simulations. Their results showed a highly synergetic effect for cooling and oxygen dilution compared with the use of a single agent. Most investigations focused on the general performance of fire suppression by water mist according to the MPS requirement, but few studies have systematically considered the effects of the spray pattern and nozzle layout on fire suppression by water mist. As such, this concept needs to be further understood to obtain optimized fire extinguishing system configuration schemes.

Therefore, the novelty and objective of the current study are to reveal the effect of spray pattern, droplet size, and nozzle layout on the application of water mist in aircraft cargo compartments. A series of case studies using a full-scale simulated aircraft cargo compartment were conducted. The Fire Dynamics Simulator 6.7.5 (FDS), developed by the National Institute of Standards and Technology, was used as the CFD tool for the modelling [42,43], which has been validated successfully in the literature [22–31,38,39,41]. The third type fire scenario-surface burning fire scenario specified in MPS was adopted. The influence mechanism of water mist parameters on fire suppression was then revealed and the optimized system parameters of nozzle and spray were obtained. This work will be helpful for the design and optimization of fire extinguishing systems in aircraft cargo compartments. The authors also encourage aircraft safety engineers and fire protection engineers to consider the aforementioned factors when designing the airborne halon replacement fire suppression systems.

2. Materials and Methods

2.1. CFD Model

The FDS code is a computational fluid dynamics model for low-speed, thermally buoyant drive flows. In the FDS, several numerical models are used: the large eddy simulation (LES) turbulent model for the gas flow produced by a fire, the eddy dissipation combustion model for fuel combustion, the Eulerian-Lagrangian two phase model for calculating the interaction between the gas phase as a continuum and water droplets as individual particles, and a thermal radiation model based on the MIE scattering theory. Detailed sub-models can be seen in the FDS Technical Reference Guide [43]. The focused theoretical models in the present study are as follows:

Extinction model. There are two extinction models in FDS to predict flame extinction, which are both based on the concept of critical flame temperature (CFT) [42,43], below which combustion cannot proceed. One extinction model considering the limiting oxygen mass fraction $Y_{O_2,lim}$ required to sustain combustion is used in this paper. $Y_{O_2,lim}$ is a simple, piecewise-linear function for local flame temperature T_f and can be written as

$$Y_{O_2,lim} = Y_{OI} \left(\frac{T_{OI} - T_f}{T_{OI} - T_\infty} \right) \quad (1)$$

where Y_{OI} and T_{OI} are the oxygen index and CFT, respectively, and T_∞ is the ambient temperature. Flame extinction is assumed if the oxygen fraction of a selected cell Y_{O_2} is less than $Y_{O_2,lim}$.

Spray model. Due to the limited ability to predict the spray atomization process by FDS, water droplets were introduced into the computational domain at a prescribed distance, r_0 , from the nozzle, using a Eulerian-Lagrangian approach. The droplet size in the actual spray was polydisperse, which is usually expressed by a probability density distribution function,

namely, cumulative volume fraction (CVF). A combination approach of the Rosin-Rammler and lognormal distributions [43] was used in the present study as follows:

$$F_{v,D_d}(D_d) = \begin{cases} \frac{1}{\sigma\sqrt{2\pi}} \int_0^{D_d} \frac{1}{\delta} \exp\left(-\frac{[\ln(D_d/D_{v,0.5})]^2}{2\sigma^2}\right) d\delta & (D \leq D_{v,0.5}) \\ 1 - \exp\left(-\ln(2)\left(\frac{D_d}{D_{v,0.5}}\right)^\gamma\right) & (D > D_{v,0.5}) \end{cases} \quad (2)$$

where $D_{v,0.5}$ is the median volumetric diameter, γ is the spread factor, and σ is a standard deviation, where $\sigma = 2/\sqrt{2\pi}(\ln 2)\gamma = 1.15/r$. σ and γ are empirical constants that can be measured by experiments, and in the current simulation, 0.48 and 2.4 were used respectively.

Heat and mass transfer model. In a real fire suppression process using a water spray system, the fire is mainly suppressed by cooling and evaporation due to interactions of the surrounding air, combustion gas, and water droplets. The heating and evaporating of droplets determine the gas-phase cooling and flammable vapor dilution effect. The mass and energy transfer during the evaporation process can be described as follows [43]:

$$\frac{dm_d}{dt} = -A_d h_m \rho_g (Y_l - Y_g) \quad (3)$$

$$\rho_g V \frac{dY_g}{dt} = -\frac{dm_d}{dt} \quad (4)$$

$$m_d c_d \frac{dT_d}{dt} = \dot{q}_r + A_d h (T_g - T_d) + \frac{dm_d}{dt} h_v \quad (5)$$

$$m_g c_g \frac{dT_g}{dt} = A_d h_d (T_d - T_g) + \frac{dm_d}{dt} (h_v + h_l) \quad (6)$$

where m_d is the mass of the droplet, kg; A_d is the surface area of the droplet, m^2 ; h_m is mass transfer coefficient; ρ_g is the gas density, kg/m^3 ; Y_l is the liquid equilibrium vapor mass fraction; Y_g is the local gas phase vapor mass fraction; V stands for the volume of a control volume, and m_g stands for mass of gas within the control volume; c_d is the liquid specific heat, $J/(kg \cdot K)$; c_g is the gas specific heat, $J/(kg \cdot K)$; h is the heat transfer coefficient between droplet and gas, $W/(m^2 \cdot K)$; \dot{q}_r is the rate of radiative heating of the droplet kW/m^2 ; h_v is the evaporation latent heat of droplet, kJ/kg ; and h_l is droplets' specific enthalpy, kJ/kg .

Fire model. Fires can be modelled in two different ways in FDS: (1) prescribe the energy released from the fuel surface; and (2) predict the energy release using the pyrolysis model [42]. The pyrolysis model was mostly used for the validation purpose of the benchmark fire. For most large-scale engineering applications, a designed fire is a simplified approximation of a real-life fire [38]. The standard t-squared model or $\tan h$ model [38,40,42] for fire growth were used to set a peak HRR value at specific time, at which the rise to a full-grown fire is achieved. Therefore, fire modeled by the first way was adopted in this paper. The heat release rate (HRR) of typical a pool fire includes three stages: fire growth, steady burning, and decay [44]. The steady burning and decay stages are controlled by suppression processes, calculated by FDS [43]. For the Jet-A pool fire, the $\tan h$ growth rate has been proven to be suitable for surface-burning fire scenario simulations [38]. In the current study, the time to reach the peak HRR was set to 60 s.

The total HRR can be calculated using the following formula [44]:

$$\dot{Q} = \dot{m}'' \Delta H_{c,eff} A_f (1 - e^{-k\beta D}) \quad (7)$$

where \dot{m}'' is the rate of localized mass loss, kg/m^2s ; $\Delta H_{c,eff}$ is the effective heat of combustion for ignition sources, kJ/kg ; A_f is the burning area of the fire source, m^2 ; $k\beta$ is an empirical constant, $3.5/m$ [38]; and D is the diameter of the oil pan, m. The mass loss rate \dot{m}'' of Jet-A was adopted from the data in reference [41].

During the interaction between water droplets and fire, except for simple heat transfer correlations, the change of the fuel pyrolysis rate induced by droplets and droplet transport on the fuel surface were also considered. The presence of water droplets would reduce the rate of pyrolysis of combustibles and then affect the total heat release rate. The total heat release is modified after spray activation [45]:

$$\dot{Q} = \dot{Q}_0 \exp(-k(t - t_0)) \quad (8)$$

where \dot{Q}_0 is the total heat release rate at the time of application t_0 ; and k is the fuel-dependent constant. This analysis is based on global water flow and burning rates. In the FDS model, the cooling of unburned surfaces and the reduction in the heat release rate are computed locally. Thus, it is awkward to apply a global suppression rule. The local heat release rate per unit area can be expressed as follows [46]:

$$\dot{q}''(t) = \dot{q}''_0(t) \exp\left(-\int k(t)dt\right) \quad (9)$$

where $\dot{q}''_0(t)$ is the burning rate per unit area of the fuel when no water is applied; and $k(t)$ is a linear function of local water mass per unit area,

$$k(t) = a\dot{m}''_w(t)s^{-1} \quad (10)$$

where $\dot{m}''_w(t)$ is the mass of water per unit area; a is the fire extinguishing coefficient. In our study, $16.4 \text{ m}^2/(\text{kg}\cdot\text{s})$ was used. based on previous studies [41].

In addition, there are two methods to simulation combustion [42,43]: one is mixing-controlled, where the reaction of fuel and oxygen is infinitely fast and controlled only by mixing; the other is the finite-rate reaction. The latter approach usually requires very fine grid resolution that is not practical for large-scale fire applications. The former simple chemistry combustion model considers a single fuel species that is composed primarily of C, H, O, and N that reacts with oxygen in one mixing-controlled step to form H_2O , CO_2 , soot, and CO. In this paper, the gas phase combustion was simplified as a single-step reaction in the simulations. As discussed in a literature review, the average molecular formula $\text{C}_{11.4}\text{H}_{21.7}$ was used as a substitute for Jet-A [38]. Therefore, the variation and effects of the system chemistry of real Jet-A in the interaction process between water droplets and fire were not considered in current study.

2.2. Case Description and Computational Setup

According to the FAA-MPS standard [6], a full-size cargo compartment simulation model of a wide-body aircraft was constructed, as shown in Figure 1. Figure 1a presents the overall layout of the testing system, and Figure 1b is a simulation scenario. The cargo compartment dimensions were $8.11 \text{ m} \times 4.16 \text{ m} \times 1.67 \text{ m}$, with a volume of 56.3 m^3 . Considering the air leak from the compartment through the cabin door and wall, a U-shaped duct with a fixed flow rate of 23.3 L/s and pipe ventilation with a leakage area of 0.00115 m^2 [38] were modeled in FDS, which would also be helpful to eliminate numerical instability for pressure solving in confined space. Three water mist nozzles as baseline cases were installed below the ceiling of the compartment, with positions of $X = 1.35 \text{ m}$, $X = 4.05 \text{ m}$, and $X = 6.75 \text{ m}$, respectively. Due to the uncertainty of a fire occurring, three fire locations were considered: a center fire, sidewall fire, and corner fire, as shown in Figure 1c. A surface burning pool fire with a size of $0.609 \text{ m} \times 0.609 \text{ m} \times 0.1 \text{ m}$ was used as a testing fire source according to the third fire scenario of MPS. As shown in Figure 1d, a thermocouple tree $T_{19}\text{-}T_{26}$ with a vertical interval of 0.2 m was positioned above the fuel pan to monitor the temperature profiles of the fire zone during the fire suppression process. Three oxygen concentration sensors were placed at different heights ($Z = 0.2 \text{ m}$, 0.8 m , 1.4 m , denoted by O_1 , O_2 , O_3) and 0.5 m away from the flame axis to monitor the changes in oxygen concentration.

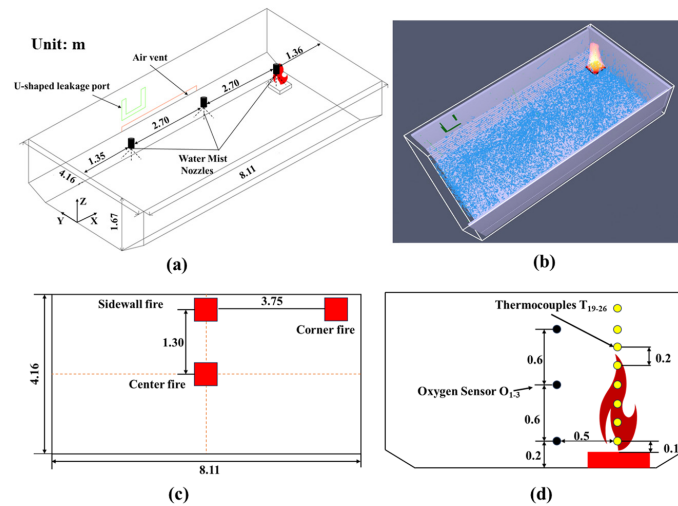


Figure 1. Schematic layout of a cargo compartment fire extinguishing system: (a) Overall layout of the testing system; (b) FDS simulation model; (c) Fire source location from top view; (d) Thermocouple and oxygen sensor system for side view.

For the simulation boundary conditions, the ambient temperature was 20 °C. The cargo wall material was double-layer standard steel, which consisted of two layers of 4-mm-thick A242 steel plate with a 100-mm air gap [38]. The spray parameters mainly included spray angle, droplet diameter, flow rate, initial droplet velocity, and atomization length. Among these, the initial droplet velocity and atomization length were fixed, and the other parameters changed for different cases. A schematic diagram of water mist spray is shown in Figure 2, where the value of α and β are the inner and outer half cone spray angle, respectively, and the total spray angle is the value of $2(\beta - \alpha)$. The spray was a solid cone for $\alpha = 0$, and the spray was a hollow cone for $\alpha > 0$. A different spray pattern could be obtained by adjusting the value of α and β . The spray patterns for $\beta \leq 90^\circ$ and $\beta > 90^\circ$ are shown in Figures 2a and 2b, respectively. In the following sections, the spray angle will be denoted by (α, β) . An increase of α means that the main spray droplets will be extended laterally, i.e., with more spray coverage and weaker average water mist flux intensity.

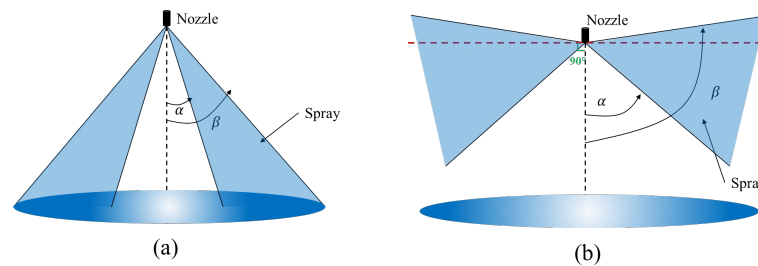


Figure 2. A schematic of the spray cone angle: (a) $\beta \leq 90^\circ$; (b) $\beta > 90^\circ$.

The nozzle number also changed from 3 to 8 considering the effects of the different nozzle layouts. The spray activation time was set as 70 s after the fuel ignition. In this study, only a Jet A fuel fire was modeled, while the piloted ignition of gasoline in FAA-MPS was not considered. The detailed properties of Jet-A are listed in Table 1. The fuel was ignited by a hot particle with a temperature of 1500 °C and lasted for 10 s, located directly above the fuel surface. In the simulation, the extinguishing criterion was set to HRR = 0. Specific cases will be introduced in the following subsections.

Table 1. Properties of the Jet-A fuel used in the simulation [38].

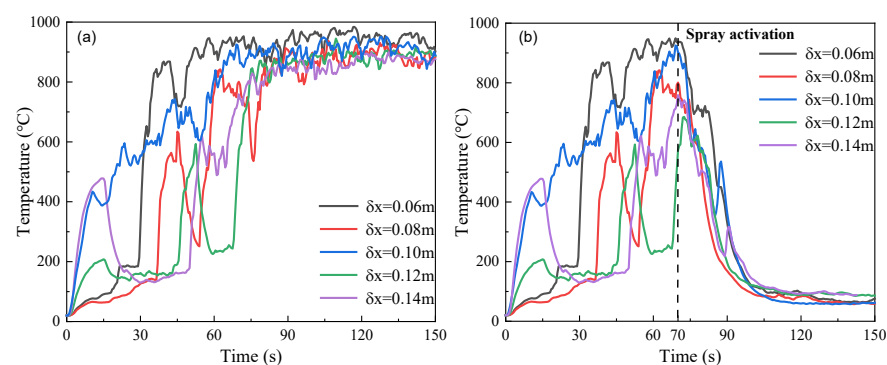
Property	Value
Molecular formula	C _{11.4} H _{21.7}
Density (kg/m ³)	820
Heat of combustion (kJ/kg)	43,000
Combustion efficiency	0.95
Heat of reaction (kJ/kg)	360
Auto-ignition temperature (°C)	250
Boiling temperature (°C)	200
Absorption coefficient (1/m)	301
Soot yield	0.097
CO yield	0.03
Radiative fraction	0.4

2.3. Grid Sensitivity Analysis

The key factor influencing the solution accuracy and computing time is the size of the computational grid specified by the user. The grid size near the fire source was initially determined by the non-dimensional expression D^*/δ_x [42], where D^* is the fire characteristic diameter and δ_x is the grid size. The fire characteristic diameter can be expressed as

$$D^* = \left(\frac{\dot{Q}}{\rho_\infty C_p T_\infty \sqrt{g}} \right)^{2/5} \quad (11)$$

where \dot{Q} is the total heat release rate from the fire source, kW; ρ_∞ is the density of air, kg/m³; C_p is the specific heat of air, kJ/(kg·K); T_∞ is the ambient temperature, K; and g is the acceleration due to gravity, m/s². The appropriate value of D^*/δ_x ranged from 4 to 16 [42]. For a corner fire of a cargo compartment, the value of \dot{Q} is about 759 kW/m² [41], whereby D^* is 0.578 m. The appropriate grid size ranges from 0.036 m to 0.1445 m. Therefore, the grid sensitivity tests with grid sizes of 0.06 m, 0.08 m, 0.10 m, 0.12 m, and 0.14 m are illustrated in Figure 3, where the temperature profiles of thermocouple T₁₉ before and after suppression were used as the monitoring point. It can be seen that the temperature variation at different scales decreased when the grid size reached 0.10 m. To minimize computational cost with sufficient accuracy, a grid size of 0.10 m was applied for further analysis.

**Figure 3.** Effect of mesh size on the data of T19: (a) without water mist; (b) with water mist.

3. Results and Discussion

The effects of fire location, spray angle, droplet size, and nozzle layout on the performance of fire suppression were identified with data collection regarding the heat release rate (HRR), temperature profile, water mist flux, and oxygen concentration profiles in the following sections.

3.1. Effects of Fire Locations on Fire Suppression Performance

The fire intensity and the hazard to the cargo compartment will be affected by the fire location. The location of the fire is uncertain, which also affects the design and performance of a fire suppression system. Therefore, cases with different fire locations (center fire, sidewall fire and corner fire) were considered, where a water flow rate of 15 L/min, initial droplet velocity of 20 m/s, the average particle size of 300 μm, and spray angles of (0°, 60°) and (30°, 90°) were used.

3.1.1. HRR and Fire Suppression Results

Figure 4 and Table 2 show, respectively, the results of the HRR variation, fire extinction time, and water consumption under different fire locations. It can be seen that for a spray angle of (0°, 60°), the fire extinction time was ranked as follows: corner fire > sidewall fire > center fire. The center fire is extinguished instantly, while the other fires were extinguished at >160 s. This was due to fact that the fire was located below the nozzle for the center fire, and most of the water droplets were concentrated on the flame. Despite the fire extinction time being close, compared with the scenario of a sidewall fire, the HRR of the corner fire was more difficult to suppress due to its greater distance from the nozzle, where the cooling effect was relatively limited. For a spray angle of (30°, 90°), the fire extinction time was ranked as follows: corner fire > center fire > sidewall fire. The fire extinction time in most cases was significantly reduced to about 40 s, which can be attributed to the more dispersed water mist flux distribution. The HRR all reduced quickly, but the HRR decay rate of the center fire was comparatively slower due to the relatively lower spray volume below the hollow spray center. Meanwhile, the HRR decay rate of the sidewall fire was faster due to more droplets expanding to both sides of the spray edge. The worst extinguishment was also observed for the corner fire for the same reason, i.e., a different fire location, which can be interpreted, combined with the cooling effect and oxygen consumption, as below. The water consumption showed a similar trend with the fire extinction time.

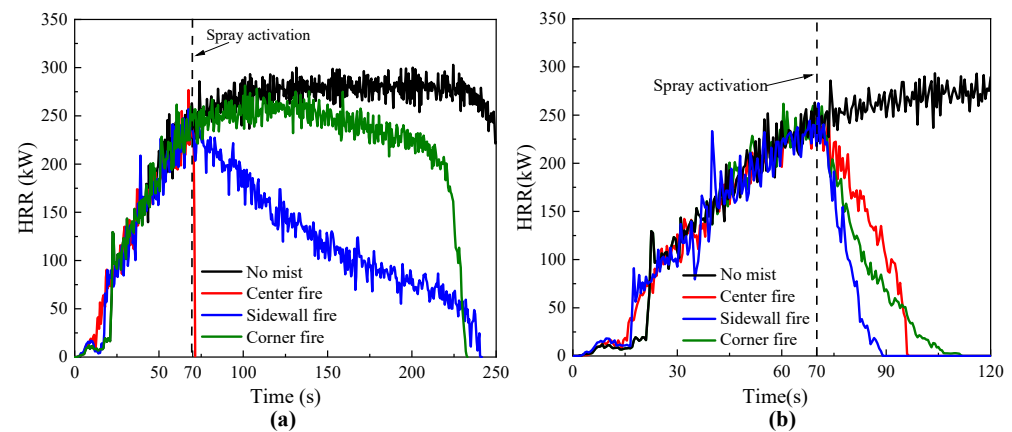


Figure 4. HRR variation results for different fire locations with spray angles: (a) (0°, 60°); (b) (30°, 90°).

Table 2. Flame extinction time and water consumption for different fire locations.

Fire Locations	Spray Angle (0°, 60°)		Spray Angle (30°, 90°)	
	Extinction Time (s)	Water Consumption(L)	Extinction Time (s)	Water Consumption(L)
Center fire	1.5	1.13	26.5	19.875
Sidewall fire	170.5	127.88	19.5	14.625
Corner fire	162.5	121.88	41.5	30.750

3.1.2. Cooling Effects Reflected by Temperature Profiles

Temperature profile is a good indication of the effectiveness of fire suppression performance. The results of centerline temperature above the fuel pan for different fire locations are shown in Figure 5. For the center fire of spray angle (0°, 60°) and sidewall fire of

spray angle ($30^\circ, 90^\circ$), the temperature of all measurement points dropped quickly after spray activation; this was caused by the dynamic effect and the relatively large water mist flux. For a center fire of spray angle ($30^\circ, 90^\circ$), due to the hollow of spray center, the temperature profiles first decreased quickly and then increased slightly, resulting from the flow field instability in suppression process. For a corner fire with spray angle ($30^\circ, 90^\circ$), the temperature profiles first decreased slightly and then kept steady for a while, which indicated that the flame could not be quickly suppressed under the limited water mist flux. In the cases of the sidewall fire and corner fire of spray ($0^\circ, 60^\circ$), the temperature profiles near the fuel source remained relatively high after spray activation, and the flame extinction time was relatively large due to the few water mist fluxes in the flame zone. The maximum temperature of T_{26} for the corner fire of spray ($0^\circ, 60^\circ$) was 411°C after spray activation for 2 min, which exceeded the acceptance criteria of 293 in MPS [6], but the other cases met the acceptance criteria. Therefore, corner fires are generally the most difficult to extinguish.

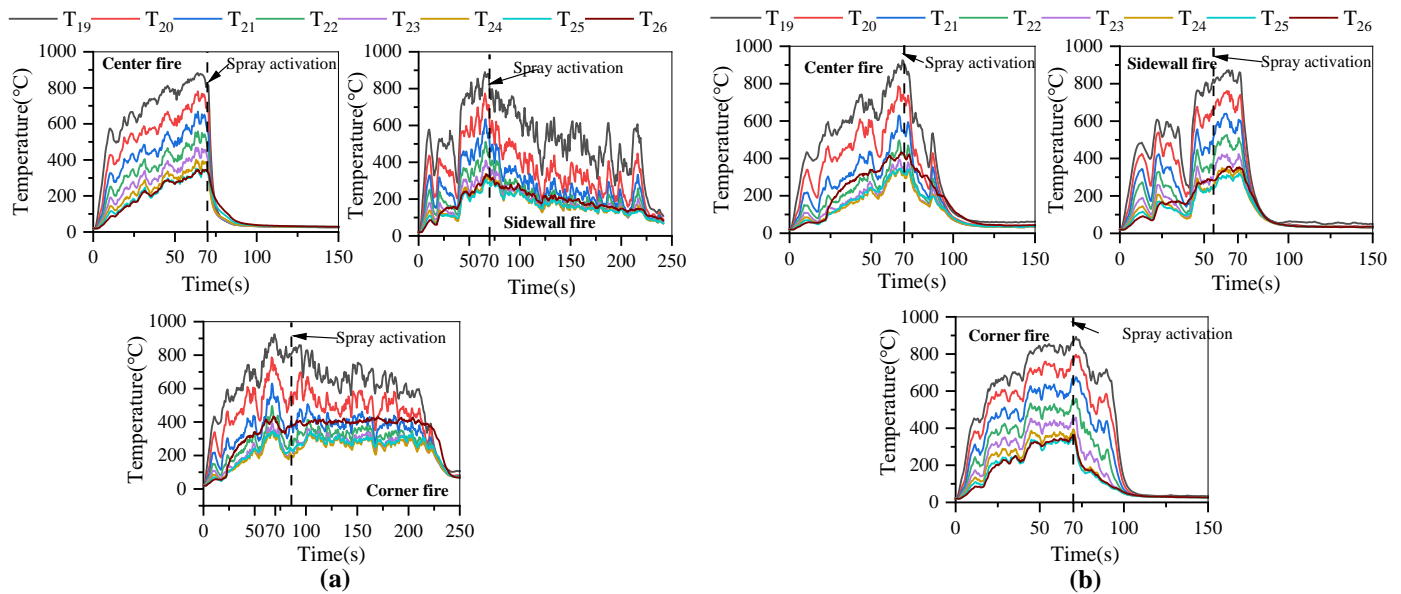


Figure 5. The centerline temperature above the fuel pan for different fire locations with spray angles: (a) ($0^\circ, 60^\circ$); (b) ($30^\circ, 90^\circ$).

The ceiling temperature is a key parameter in evaluating the thermal protection characteristics of water mist. Figure 6 shows the ceiling temperature distribution at the time of 0 s, 5 s, 15 s after spray activation. As shown, the ceiling temperature distribution had a similar trend with the flame temperature variation. For cases of no water mist, the corner fire scenario had the largest high temperature zone due to the wall restrictions. At 5 s after spray activation, the ceiling temperature of the center fire scenario dropped rapidly and the maximum temperature was 125°C for spray angle ($0^\circ, 60^\circ$) and 150°C for spray angle ($30^\circ, 90^\circ$). In the case of corner fires, the ceiling temperature only decreased slightly and still remained relative high, with the maximum temperature exceeding 293°C . At 15 s after spray activation, the ceiling temperature dropped to below 100°C for the center fire of ($0^\circ, 60^\circ$) and sidewall fire of ($30^\circ, 90^\circ$). For corner fires, the ceiling temperature decreased more significantly under spray angle ($30^\circ, 90^\circ$) than under spray angle ($0^\circ, 60^\circ$) due to the relatively large coverage area of the water droplets.

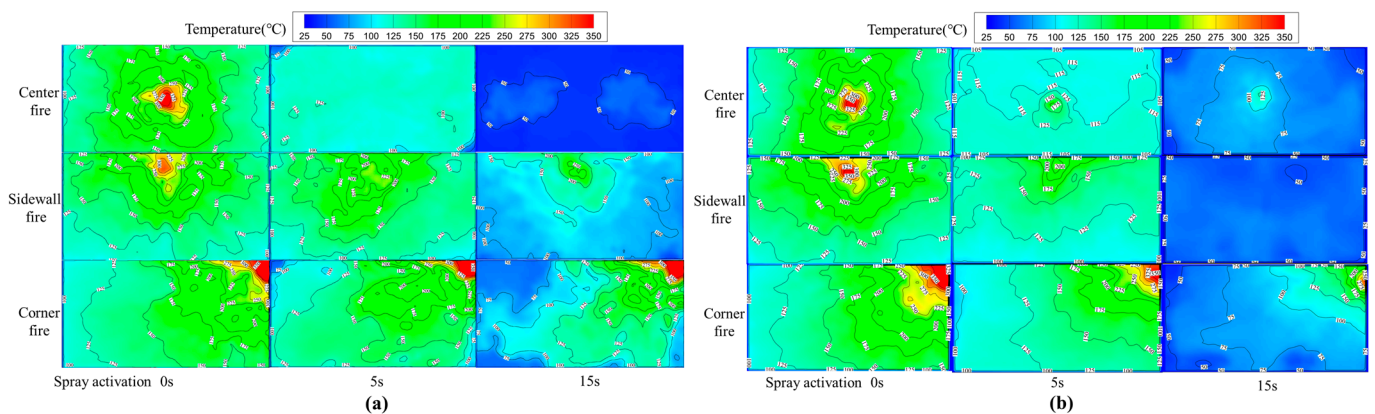


Figure 6. The ceiling temperature distribution for different fire locations with spray angles: (a) (0° , 60°); (b) (30° , 90°).

3.1.3. Oxygen Concentration Profiles

The above analysis concentrated on the suppression mechanism of the cooling effect, while the mechanism of oxygen dilution is also one key factor that determines flame extinction. In the process of fire suppression, water droplets will evaporate into vapor when heated and then expand in volume to exceed three orders of magnitude of the original volume of water droplets [9]. This expansion in volume can subsequently disrupt the entrainment of air into the flame and lead to the reduction of the oxygen concentration in the flame zone, when the value reaches the limiting oxygen concentration, and flame extinction will occur. The oxygen concentration results, measured by an oxygen sensor (O_1 , O_2 and O_3) for different fire locations are shown in Figure 7. For all cases before spray activation, the oxygen concentration at the upper measuring point decreased firstly due to the accumulation of upper smoke gas. With the moving down of the smoke gas layer, the oxygen concentrations at the lower measuring points gradually decreased. The reduction of the oxygen concentration decreased from top to bottom, which was caused by the stratification of smoke gas with a large amount of smoke accumulating in the upper region. Meanwhile, the oxygen concentration variation curve shows some fluctuation for the upper oxygen sensor (O_3) due to the unsteady movement of smoke. After suppression began, oxygen concentrations at the lower and middle points dropped quickly, since the smoke sank due to water mist injection. In most cases, the oxygen concentration decay curves basically coincided after a while until fire extinction. However, oxygen concentrations at the upper point (O_3) showed a relative lower value and varied with the fire location and spray angle. For a spray angle of (0° , 60°), the oxygen concentration of O_3 for the center fire increased instantly due to very short extinction time, while the value for the sidewall and corner fires continued to decrease until the flame was extinguished, with minimum oxygen concentrations reaching about 15% and 11%, respectively. For a spray angle of (30° , 90°), the oxygen concentration of O_3 dropped first and then increased until fire extinction, with minimum oxygen concentrations reaching about 15–16.5%. After suppression, due to the falling temperature and forced ventilation, ambient air entered the compartment through the pipes in the sidewall, which led to an increase in oxygen concentration, which eventually stabilized at around 18%.

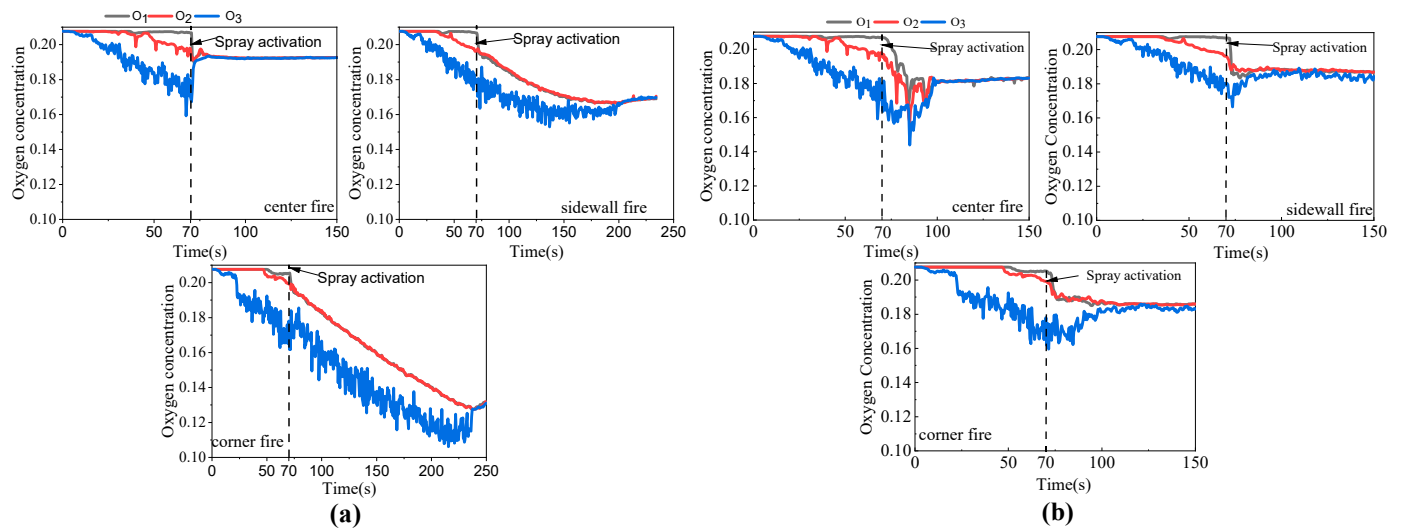


Figure 7. Oxygen concentration results for different fire locations with spray angle: (a) (0° , 60°); (b) (30° , 90°).

From the above, it can be concluded that the fire suppression performance of water mist was not only affected by the distance between fire location and nozzle, but also by the injection angle of the spray. The effects of spray angle will be further identified and analyzed in detail below. In addition, since the corner location was found to be the most difficult to extinguish, corner fires are considered as scenarios to evaluate the fire suppression performance by water mist in the following sections.

3.2. Effects of Spray Pattern on Fire Suppression Performance

The spray atomization angle determines the water coverage area and the mist flux distribution in the fire zone. In this part, the two spray patterns related to solid spray and hollow spray were considered. Only the value of β changed for the solid spray, while the value of α and of $(\beta - \alpha)$ was fixed as 60° , with subsequent changes of the value of α for a hollow spray. The parameters such as the flow rate (15 L/min), initial droplet velocity (20 m/s), and average particle size (300 μm) were fixed. The solid spray with angles of (0° , 45°), (0° , 60°), (0° , 90°), (0° , 105°), and (0° , 120°), and the hollow spray with angles of (0° , 60°), (15° , 75°), (30° , 90°), (45° , 105°), and (60° , 120°) were selected in the study.

3.2.1. Contours of Water Mist Flux Distribution

In order to identify the spray coverage properties under different spray angles in a cargo compartment, the contours of water mist flux distribution on the sampling plane at $Z = 0.2$ m above floor were extracted in the steady stage of an individual spray without fire, as shown in Figure 8. The water mist flux is the mass of water droplets per unit volume in kg/m^3 . From Figure 8a, it may be observed that for the solid spray, most droplets were concentrated at the center, resulting in a smaller coverage area, even for large spray angles. This can be attributed to the fact that small droplets carry much less momentum with a smaller mass, and the droplets lose momentum quickly due to the drag from air. Thus, they cannot follow the intended trajectory and travel along horizontal distances, especially for the suppression scenarios involving additional fire thermal buoyancy. With the value of β increasing, the spray coverage area increased slightly and then remained invariant basically when the value of β exceeded 90° . The water mist flux intensity decreased from a maximum value of $0.12 \text{ kg}/\text{m}^3$ with (0° , 45°) to $0.06 \text{ kg}/\text{m}^3$ with 0° , 120° . This was because the larger coverage area for a large spray angle led to a smaller water mist flux per unit area, with the assumption of fixed flow rate. As shown in Figure 8b, for a hollow spray, the spray coverage area increased significantly, and the largest spray coverage area was observed at the spray angle of (45° , 105°), which is essential to extinguish any possible fire

in a cargo compartment. With an increase of α , the spray coverage area increased, and the average water mist fluxes decreased, but the fluxes of water mist below the center of the nozzle were the smallest due to no droplets being injected from the nozzle. However, a part of the spray was injected toward the cargo ceiling when the value of β exceeded 90° (also seen in Figure 2b), and then the droplets in this part fell directly to the floor. Therefore, the water mist flux of the center region increased with spray angles of $(45^\circ, 105^\circ)$ and $(60^\circ, 120^\circ)$.

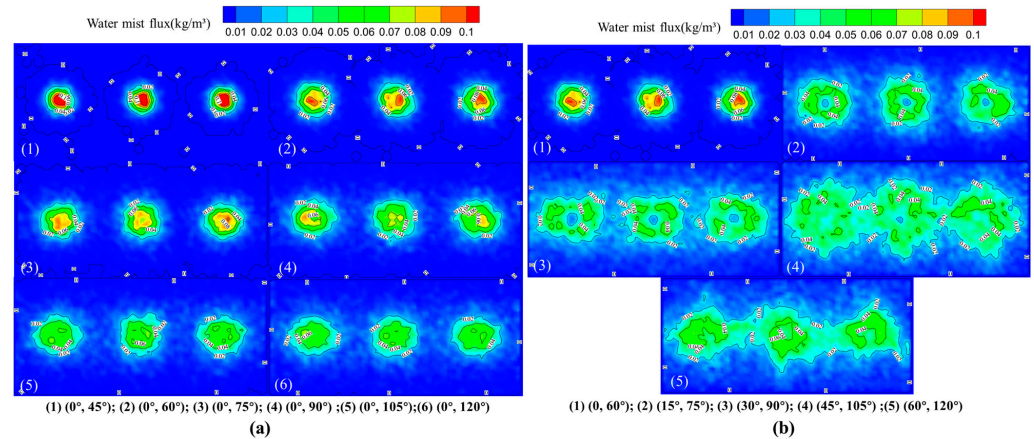


Figure 8. The contours of water mist flux on the sampling plane at $Z = 0.2$ m: (a) Solid spray; (b) Hollow spray.

The typical contours of droplet velocity on the sampling plane at $Y = 0.0$ m are shown in Figure 9. For a solid spray, the velocity of spray body decreased with an increase of spray angle, and a high velocity occurred in the center of the spray. This can be interpreted as evidence that the axial velocity of droplets will decrease toward the spray edge and the radial velocity of droplets will decay rapidly due to air drag with an increase of spray angle, with most droplets eventually concentrating in the spray center body. For the hollow spray, the velocity of spray body reduced significantly, especially for the axial velocity with β exceeding 90° , where the droplets with high velocity were mainly concentrated in the region below the cargo ceiling, before falling down with a low velocity. This was because the axial velocity of most droplets decreased, and some droplets had an upward velocity with β exceeding 90° . Meanwhile, the radial velocity of the droplets increased due to the changes of injection direction, which all resulted in a concentration of droplets in the upper region after spray activation.

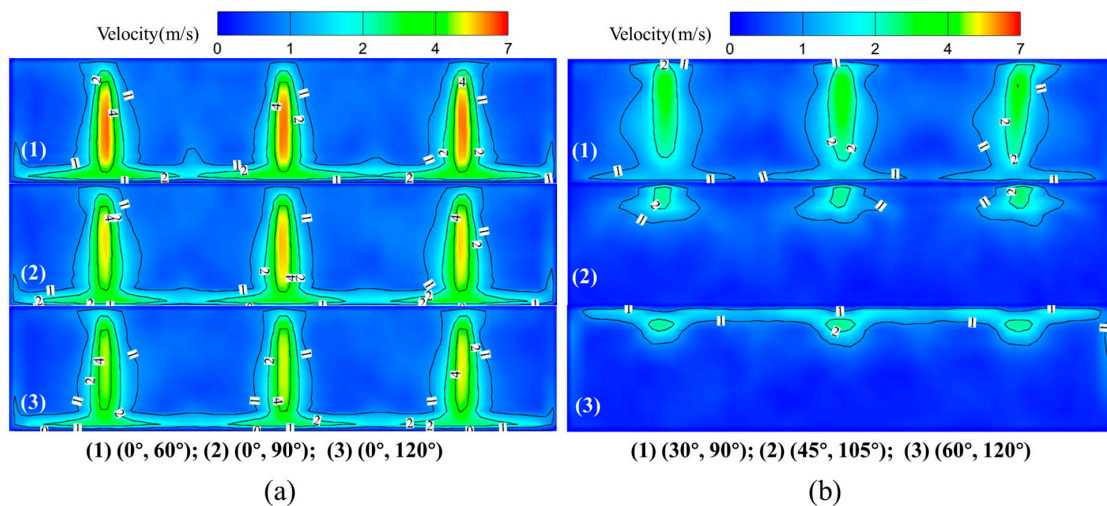


Figure 9. Contours of droplet velocity on the sampling plane at $Y = 0.0$ m: (a) Solid spray; (b) Hollow spray.

3.2.2. HRR and Fire Suppression Results

Figure 10 and Table 3 show, respectively, the results of HRR variation, fire extinction time, and water consumption under different spray patterns. It can be seen that the HRR decay rate was relatively smaller, and the fire extinction time was relatively larger for the cases of solid spray compared with the cases of hollow spray. The minimum extinction time was 104.0 s for the former, and the maximum extinction time was 72.0 s for latter. In the case of the solid spray, the HRR data reduced, and the fire extinction time first increased and then decreased with an increase of β . At a spray angle of $(0^\circ, 45^\circ)$, the HRR under the suppression stage was almost unaffected by the water mist, which indicated that the cooling effect of spray was almost nil owing to very low droplet penetration. However, the fire extinction time was reduced to 152.5 s for the enhancement of the oxygen dilution effect compared with no mist. Increasing the value of β , the fire extinction time increased and the maximum value occurred at around 75° of β . This could be attributed to the fact that the cooling effect increased, resulting from more droplet penetration, but the oxygen consumption of fuel combustion also decreased due to the reduction of the HRR rate, which both caused longer flame burning times. With continuing β , the quantity of droplets entering the flame region increased due to relatively large spray coverage, and the cooling effect was dominant in the suppression, leading to a reduction of flame extinction.

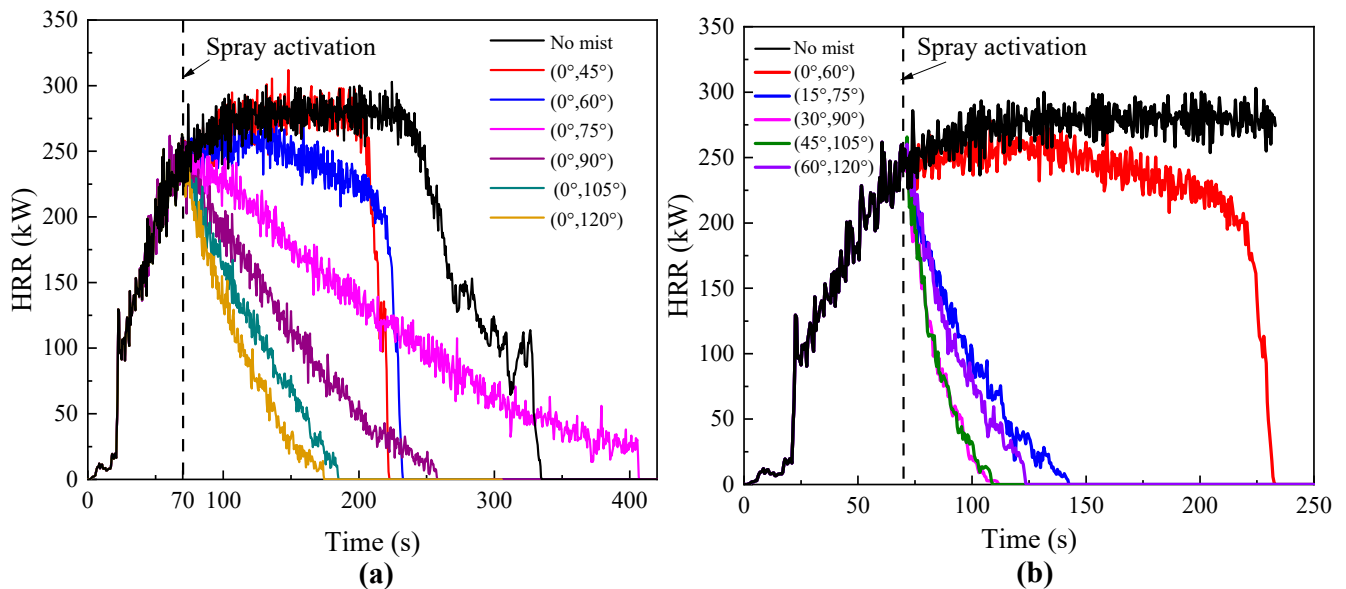


Figure 10. HRR variation results for different spray patterns: (a) Solid spray; (b) Hollow spray.

Table 3. Fire extinction time and water consumption for different spray patterns.

Solid Spray	Extinction Time (s)	Water Consumption (L)	Hollow Spray	Extinction Time (s)	Water Consumption (L)
$(0^\circ, 45^\circ)$	152.5	114.38	$(0^\circ, 60^\circ)$	162.5	121.88
$(0^\circ, 60^\circ)$	162.5	121.88	$(15^\circ, 75^\circ)$	72.0	54.00
$(0^\circ, 75^\circ)$	337.0	252.75	$(30^\circ, 90^\circ)$	41.5	30.75
$(0^\circ, 90^\circ)$	187.5	140.63	$(45^\circ, 105^\circ)$	39.5	29.25
$(0^\circ, 105^\circ)$	114.5	85.86	$(60^\circ, 120^\circ)$	54.0	40.50
$(0^\circ, 120^\circ)$	104.0	78.00	/	/	/

For the hollow spray, the HRR decay rate increased and fire extinction time first decreased and then increased with an increase of α . The significant reduction in HRR and fire extinction time with the spray angle from $(0^\circ, 60^\circ)$ to $(15^\circ, 75^\circ)$ indicated that the hollow spray showed better fire suppression performance compared with the solid spray, which can be interpreted combined with Figure 8b, where the former had a larger spray coverage

area and more uniform water mist flux distribution. And the cases for spray angles of (30°, 90°) and (45°, 105°) showed the best fire suppression performance, with extinction times of about 40 s. This could be attributed to the fact that more droplets involved in the flame cooling process were present due to the relative larger spray coverage area. The results of water consumption showed a similar trend to that of the fire extinction time.

3.2.3. Cooling Effects Reflected by Temperature Profiles

The typical temperature results of thermocouple T₁₉, T₂₂, and T₂₅, corresponding to positions of 0.2 m, 0.8 m, and 1.4 m above the fuel pan for different spray patterns, are presented in Figure 11. It can be observed that most of the temperature profiles shared similar behavior with the HRR results. Compared with the cases of solid spray, the cases of hollow spray showed better cooling effects, where all points showed relatively lower temperature after spray activation. For the solid spray, the temperature of T₁₉ was relatively larger for all cases, and the temperature decay rate increased with an increase of β , while the temperature in the middle and upper positions first decreased and then increased to a steady state for $\beta < 90^\circ$. This could be attributed to the fact that the flame was quickly suppressed under the droplet impaction and cooling effect after the spray activation, but the flame again increased in intensity, induced by the thermal buoyancy of the flame due to a weak water mist flux. Eventually, the interaction between spray and flame reached a balance, leading to flame extinction. For $\beta \geq 90^\circ$, the water mist flux entering the flame zone increased owing to the relatively larger spray coverage, and then the temperature at all points decreased gradually until fire extinction. For the hollow spray, the temperature at all points decreased quickly after spray activation due to the large spray coverage, but the temperature decay rate for spray angle of (60°, 120°) was the smallest, owing to the relatively weak droplet downward velocity and water mist flux.

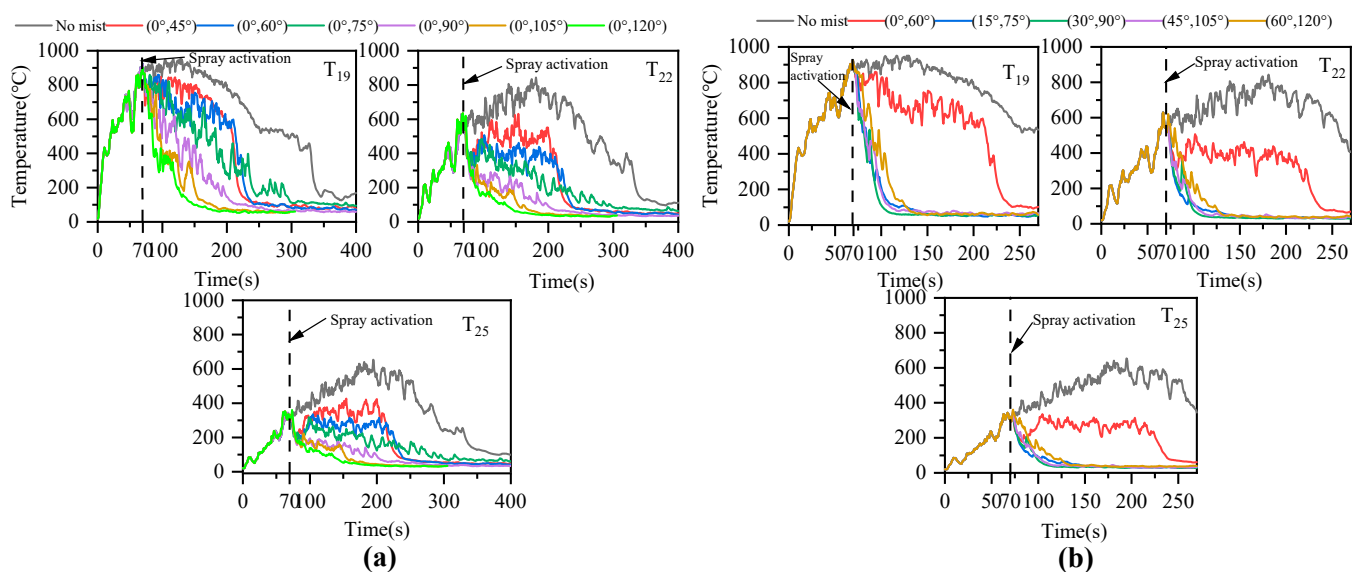


Figure 11. Temperature profiles of thermocouple T₁₉, T₂₂, and T₂₅: (a) Solid spray; (b) Hollow spray.

Figure 12 shows the ceiling temperature distribution results at times of 0 s, 5 s, and 15 s after spray activation for different spray patterns. The ceiling temperature distribution showed a similar trend with the flame temperature variation. It should be noted that the result for the case of no mist is presented in Figure 12b, where the maximum ceiling temperature was about 450 °C at the region above the flame; then, the temperature gradually decreased in all directions. For the solid spray, the ceiling temperatures of most cases were still relatively high, with the maximum temperature exceeding 400 °C for $\beta \leq 90^\circ$ and just decreasing slightly in the region far from the fire position. This could be attributed to the fact that most droplets were concentrated in the middle region of the floor, combined with

the water mist flux distribution shown in Figure 8a, and the part of droplets entering into the fire plume was not enough to cool the thermal plume. However, the for hollow spray, the ceiling temperatures for most cases were reduced significantly and even changed α by 15° from 0° to 15°, where the maximum ceiling temperature was reduced to about 370 °C from 450 °C. The cases of spray angle (30°, 90°) and (45°, 105°) presented the best cooling effect, and the ceiling temperatures decayed better with an increase of α for the ceiling region far from the fire; this can be attributed to the presence of more droplets concentrated in the area below the ceiling.

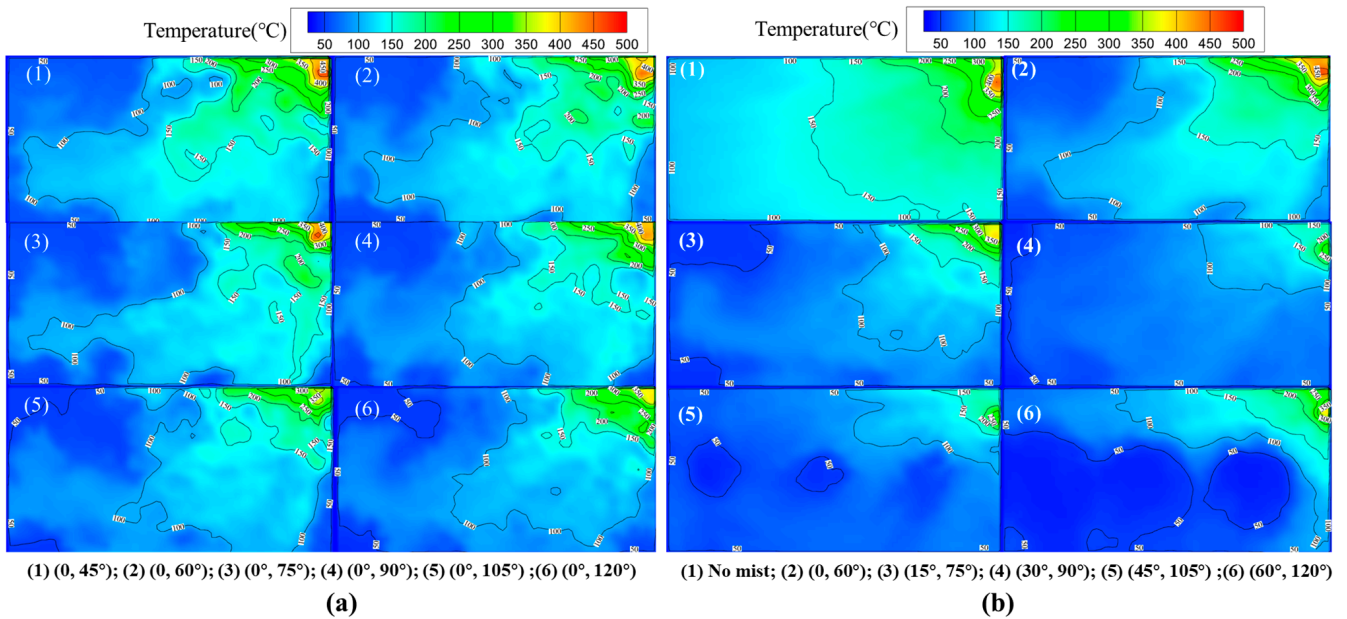


Figure 12. Ceiling temperature distribution at 15 s after spray activation: (a) Solid spray; (b) Hollow spray.

3.2.4. Oxygen Concentration Profiles

The oxygen concentration profiles of the O₁ oxygen sensor for different spray patterns are shown in Figure 13. The O₁ data indicate oxygen concentration variation at the low position near the base of the fire. The oxygen concentration first decreased rapidly in all cases after spray activation, and the decay rate was larger than the case of no mist. This could be attributed to the fact that the downward droplets entrained the smoke gas from the upper layer to the lower layer and the small droplets also diluted the oxygen volume fraction in the air, which both led to a decrease in the oxygen concentration. For the solid spray, the oxygen concentration decay rate showed the same trend for all cases before about 37 s after spray activation and then gradually reduced with an increase of β due to the increasing spray coverage area. In addition, the oxygen concentration value at the flame extinction also increased with an increase in β . For the hollow spray, the minimum oxygen concentrations were relative larger than for the cases of the solid spray, and a rise stage in the fire suppression could be observed due to the spray dynamic inducing air flow. For the cases of (30°, 90°) and (45°, 105°), the final oxygen concentrations were relatively larger, resulting from faster fire extinction, which further indicated that the cooling effect has been enhanced.

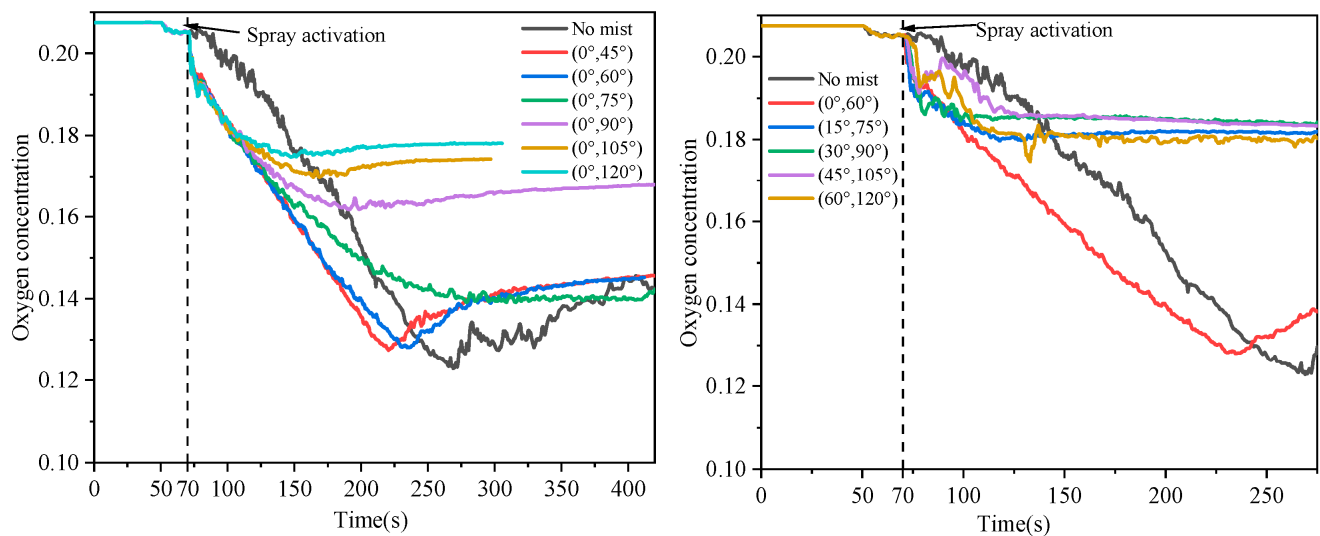


Figure 13. Oxygen concentration results of the O₁ oxygen sensor for different spray patterns.

3.3. Effects of Droplet Size on Fire Suppression Performance

In order to investigate the effect of droplet size on the fire suppression performance by water mist in a cargo compartment, a flow rate of 15 L/min, an initial droplet velocity of 20 m/s, a spray angle of (30°, 90°), and average droplet diameters of 50 μm, 100 μm, 150 μm, 200 μm, 250 μm, 300 μm, 350 μm, and 400 μm were applied in the simulations.

3.3.1. The Contours of Water Mist Flux Distribution

The contours of the water mist flux density for different droplet sizes on the sampling plane at $Z = 0.2$ m above floor are presented in Figure 14. It can be observed that the water mist flux distribution, including spray coverage area and flux density, was significantly affected by variations in the droplet diameter. Here, a contour value of 0.01 kg/m³ could be used as the outer boundary of the spray coverage. With increasing droplet diameter, the spray coverage area increased and the water mist fluxes at the center below nozzle decreased and gradually diffused to the surrounding edge area. For small droplet diameters, most droplets concentrated in the center region below the nozzle despite the hollow cone spray, and the maximum water mist flux density for a droplet diameter of 50 μm was about 0.5 kg/m³. When the droplet diameter reached 200 μm, the water mist flux density reduced significantly and the maximum water mist flux shifted outward in the radial direction. For a droplet diameter of 300 μm, the spray coverage area was basically close to the cargo compartment floor area, but the water mist flux at the center below the nozzle became very small. With the droplet diameter continuing to increase to 400 μm, the water mist flux density in the central region was close to 0, and the region with a small mist flux also expanded. Meanwhile, the overall water mist flux intensity decreased significantly and became more dispersed. This could be attributed to the fact that the velocity of small droplets decayed more easily due to the drag from air; then, most droplets dropped down after traveling short distances in a radial direction for the same initial velocity.

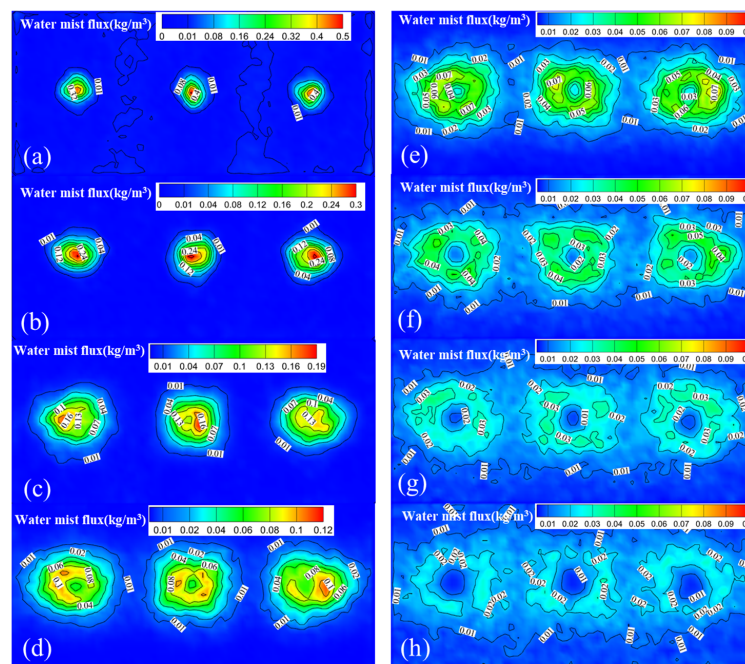


Figure 14. The contours of water mist flux on the sampling plane at $Z = 0.2$ m for different droplet sizes: (a) $50 \mu\text{m}$; (b) $100 \mu\text{m}$; (c) $150 \mu\text{m}$; (d) $200 \mu\text{m}$; (e) $250 \mu\text{m}$; (f) $300 \mu\text{m}$; (g) $350 \mu\text{m}$; (h) $400 \mu\text{m}$.

As a large mass can overcome air resistance better, such water mist droplets can travel long horizontal distances, and the maximum water mist flux region may be shifted outward. The spray coverage also increases with an increase in the droplet diameter. A visualization of such a water spray is shown in Figure 15, further validating our analysis, where the spray body was narrower with an average droplet diameter of $50 \mu\text{m}$ and the spray body became more divergent with a droplet diameter of $400 \mu\text{m}$.

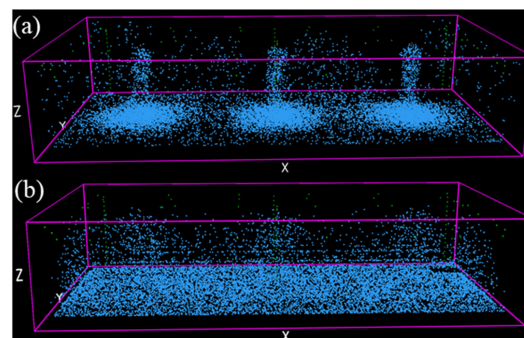


Figure 15. Visualization of water mist droplets by Lagrange particles for different average droplet diameters: (a) $50 \mu\text{m}$; (b) $400 \mu\text{m}$.

3.3.2. HRR and Fire Suppression Results

Figure 16 and Table 4 show, respectively, the results of HRR variation, fire extinction time, and water consumption under different droplet sizes. It can be seen that with increasing droplet diameter, the performance of fire suppression first decreased and then increased; the fire suppression efficiency was the worst at the droplet diameter of $200 \mu\text{m}$ with a maximum value of 186.5 s for the extinction time and 139.88 L of water consumption. The HRR data for droplet diameters of 50 – $150 \mu\text{m}$ still maintained large values. This was because for small droplet sizes, the water droplets evaporated quickly, and it was difficult for the water droplets to penetrate the flame zone due to their concentration in the center region and low momentum. Therefore, the cooling effect was relatively weak, and the oxygen displacement with a similar effect to that of a gas extinguishing agent was

dominant, leading to the large HRR. For a droplet diameter of 50 μm , the vaporization effect was the strongest and the extinguishing time was relatively short due to the strong suffocation effect. For a droplet diameter ≥ 250 μm , the HRR data decreased quickly after spray activation and the decay rate increased gradually with increasing droplet diameter. Also, the cooling effect became the dominant fire extinguishing mechanism. For a droplet diameter of 250 μm , the fire extinction time was reduced to 67 s, being smaller than the case of 50 μm , where the spray coverage was relatively large and more droplets entered the flame zone. As the droplet size continued to increase to 350 μm , the fire extinction time was reduced to 26.5 s and became invariant with the droplet size, which indicated a the size of 350 μm may be optimal. For the case of a droplet diameter of 200 μm , both the suffocation effect and the cooling effect simultaneously dominated fire suppression, leading to the extenuation of the extinguishing time. This could be attributed to fact that the fuel pyrolysis rate reduced due to the cooling effect, and then oxygen consumption, required to maintain combustion, was reduced. At the same time, the fire suppression effect by suffocation effect also became weak, eventually leading to poor suppression performance. The results of water consumption also showed a similar trend with the fire extinction time.

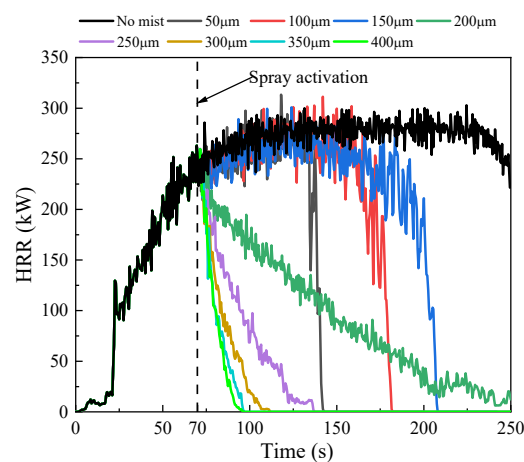


Figure 16. HRR variation results for different droplet diameter.

Table 4. Fire extinction time and water consumption for different droplet sizes.

Average Droplet Diameter (μm)	Extinction Time (s)	Water Consumption (L)
50	72.5	54.38
100	112.0	84.00
150	138.0	103.50
200	186.5	139.88
250	67.0	50.25
300	41.5	30.75
350	26.5	19.88
400	26.0	19.50

3.3.3. Cooling Effects Reflected by Temperature Profiles

Figure 17 shows the typical temperature profiles of T_{19} , T_{22} , and T_{25} for different average droplet sizes. It can be observed that for droplet diameters ranging from 50 to 150 μm , the temperature of each position first decreased slightly after spray activation and then was accompanied by a sudden temperature rise phenomenon, subsequently stabilizing at a higher temperature until the flame was extinguished. This was attributed to the fact that the flame was quickly suppressed under the spray dynamic effect and cooling effect but then rose again due to a weak water mist flux in the flame zone. For a droplet larger than 200 μm , the cooling rate increased significantly, and the temperature of each position decreased greatly. The same explanation as with the HRR results analysis applies here.

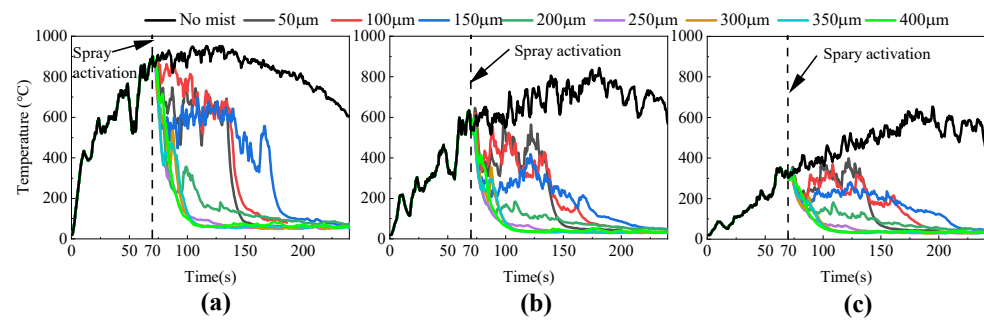


Figure 17. The temperature profiles above the fuel pan: (a) T_{19} ; (b) T_{22} ; (c) T_{25} .

Figure 18 shows the results of the ceiling temperature distribution at 15 s after spray activation. The overall ceiling temperature of the cargo compartment also showed a similar trend as that HRR data with an increase in the droplet diameter. For a droplet diameter of 150 μm , the maximum temperature at the region above the flame was about 500 $^{\circ}\text{C}$, and the ceiling temperature decreased significantly, with a maximum temperature of 250 $^{\circ}\text{C}$ when the droplet diameter was increased to 300 μm . However, the temperature at the region far from the fire decreased continuously with an increase in the droplet diameter. This could be attributed to the fact that for small droplets with less momentum, most droplets could not travel long distances in the radial direction, leading to their concentration in the center region below the nozzle, which weakened the cooling effect in the total cargo compartment. Meanwhile, large droplets with higher momentum could pass through the smoke gas layer and flame zone, and thus, the cooling effect was stronger.

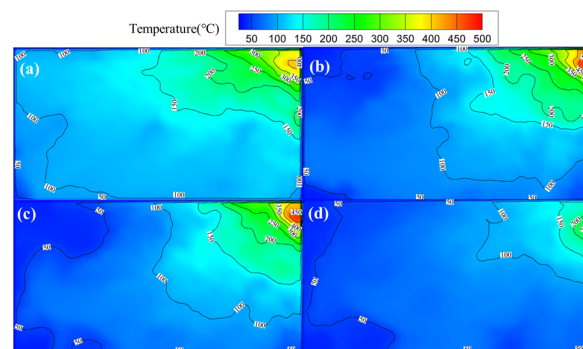


Figure 18. Ceiling temperature distribution at 15 s after spray activation: (a) 50 μm ; (b) 150 μm ; (c) 200 μm ; (d) 300 μm .

3.3.4. Oxygen Concentration Profiles

The oxygen concentration profiles of the O_1 oxygen sensor for different droplet sizes are shown in Figure 19. The decay rate of the oxygen concentration for a droplet diameter of 50 μm was the largest. The oxygen concentration for case of 150 μm was the lowest, with a value about 13.5% due to the long extinction time. This further verified the above analysis, i.e., that the high production of water vapor due to the vaporization effect led to a high oxygen displacement in the cargo compartment, which caused a large decay rate in the oxygen concentration. For large droplets, such as droplet diameter of 300 μm , due to the short extinction time of 41.5 s, the oxygen concentration was about 18.5% before the fire extinction. The decay rate in the oxygen concentration was reduced where the cooling effect was dominant, and the suffocation effect was weakened.

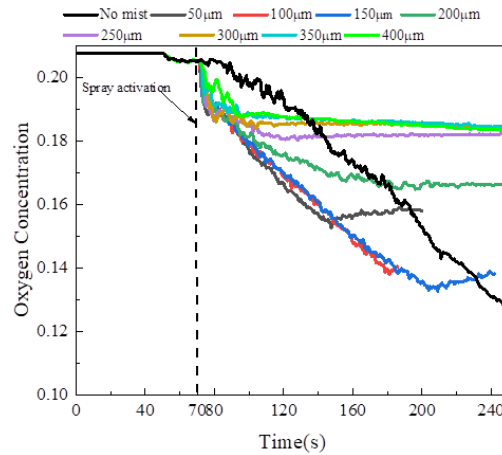


Figure 19. Oxygen concentration results of the O₁ oxygen sensor for cases of different droplet sizes.

3.4. Effects of Nozzle Layout on Fire Suppression Performance

From the above sections, it can be observed that the spray generated by three nozzles installed under the ceiling could not cover the overall area of the cargo floor in most cases, which could make it impossible to extinguish a fire in any location in an actual aircraft cargo compartment. Therefore, it was necessary to further explore the effects of nozzle layout on fire suppression performance, with the aim of obtaining better fire extinguishing parameters. Therefore, five types of nozzle layout were applied, as shown in Figure 20, with nozzle numbers 3, 4, 5, 6, and 8, respectively. A water flow rate of 10 L/min, an initial droplet velocity of 20 m/s, an average droplet diameter of 300 µm, and a spray angle of (30°, 90°) were used.

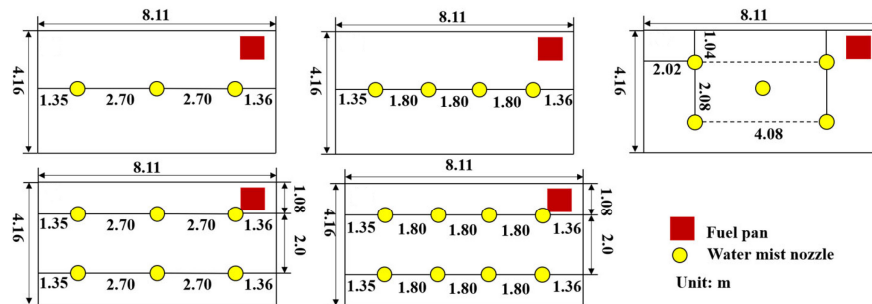


Figure 20. Schematic of Nozzle Layouts.

3.4.1. The Contours of Water Mist Flux Distribution

Figure 21 shows the contours of water mist flux on the sampling plane at $Z = 0.2$ m for different nozzle layouts. With an increase in nozzle number, the distribution of the water mist flux became more uniform, and the water mist flux density and spray coverage area increased accordingly. Increasing one nozzle, the water mist could cover the total middle region and the entire floor, except for both sides of the center region for 5 nozzle layouts. When the number of nozzles increased to six, it could be seen that the spray covered almost the entire floor area of the cargo compartment. For 8 nozzles, the water completely covered the whole bottom area of the cargo floor and the water mist flux density was relatively large. In the actual fire suppression of a cargo compartment, the optimal nozzle configuration scheme needs to consider the influence of water consumption and fire extinguishing time.

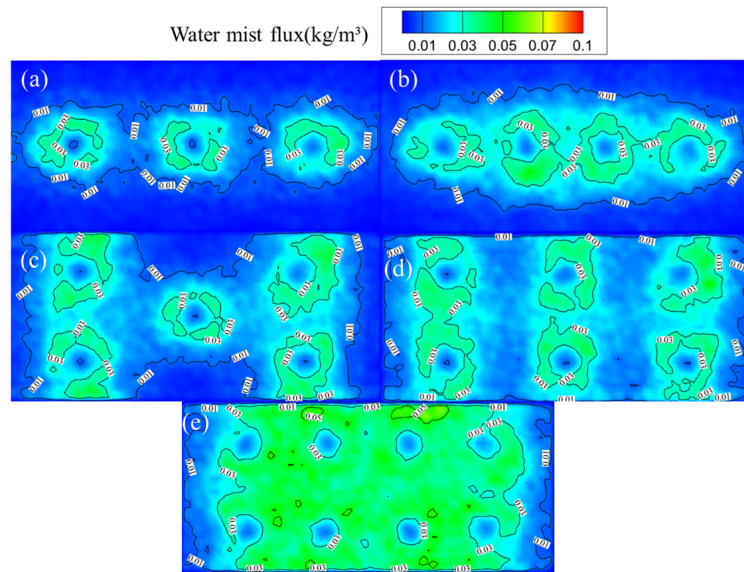


Figure 21. The contours of water mist flux on the sampling plane at $Z = 0.2$ m with different nozzle layouts: (a) 3; (b) 4; (c) 5; (d) 6; (e) 8.

3.4.2. HRR and Fire Suppression Results

Figure 22 and Table 5 show, respectively, the results of HRR, fire extinction time, and water consumption under different nozzle layouts. It can be observed that the HRR decay rate increased with increasing nozzle number. The HRR decay rate for 4 nozzle layouts was similar to that with 3 nozzle layouts, but the fire extinction time of the former was reduced by 22.14% compared with the latter, which indicated that the cooling effect was similar but the suffocation effect was larger for the former due to the introduction of more droplets. Continuing to increase the number of nozzles to 5, the HRR decay rate increased significantly, the fire extinction time was reduced to 22 s, and a decrease of about 74.47% compared with 3 nozzles was observed, which indicated that the cooling effect had been enhanced significantly due to the large spray coverage. Then, the HRR decay rate further increased and the fire extinction time was reduced to about 14 s for both the 6 and 8 nozzle layouts; however, the water consumption of the former was the lowest. Therefore, the optimal number of nozzles was found to be 6 for the current fire suppression scenario.

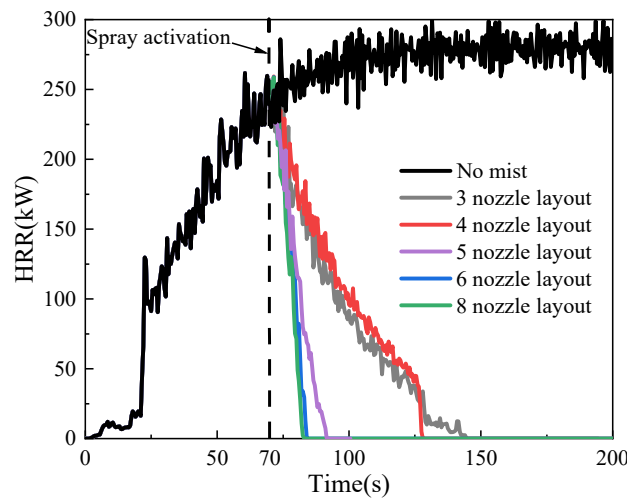


Figure 22. HRR variation results for different nozzle layouts.

Table 5. Fire extinction time and water consumption for different nozzle layouts.

Nozzle Number	Extinguishing Time (s)	Water Consumption (L)
3	74.5	37.25
4	58.0	38.67
5	22.0	18.33
6	14.5	14.50
8	13.0	17.33

The water flow rate is another key parameter which determines the total amount of water droplets injected from the nozzle directly. Therefore, layouts of 5, 6, and 8 nozzles and water flow rates of 8, 10, 12, 14, and 16 L/min were used in our simulation. As shown in Figure 23, an increase in the water flow rate reduced the fire extinguishing time significantly, while the variation in water consumption was not significant. The water consumption with 6 nozzles was the lowest compared with the other nozzle layouts. The fire extinguishing time was close for the 6 and 8 nozzle layouts, while the latter consumed more water, especially for larger water flow rates.

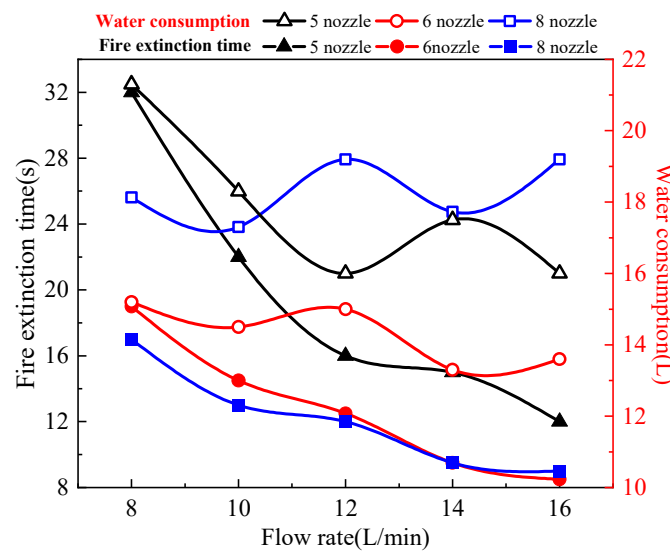


Figure 23. Fire extinction times and water consumption for different water flow rates.

3.4.3. Cooling Effects Reflected by Temperature Profiles

Figure 24 shows the temperature profiles of T_{19} , T_{22} , and T_{25} for different nozzle layouts. It can be seen that the temperature of each position decreased rapidly after spray activation. The cooling rates of the 5, 6, and 8 nozzle layouts were close and increased significantly compared with those of the 3 and 4 nozzle layouts, which indicated that a 5-nozzle layout had a good enough fire suppression performance for the corner fire. The ceiling temperature distribution at 5 s and 15 s after spray activation is shown in Figure 25. The overall ceiling temperature in the cargo compartment also showed a similar trend to that of HRR with an increase in nozzle number. At 15 s after spray activation, the cases of the 3 and 4 nozzle layouts still had relatively higher ceiling temperatures, while the ceiling temperature showed an obvious decrease for the 5-nozzle layout. In contrast, the ceiling temperatures in the cases of the 6 and 8 nozzle layouts reduce to the ambient temperature, showing a significant cooling effect.

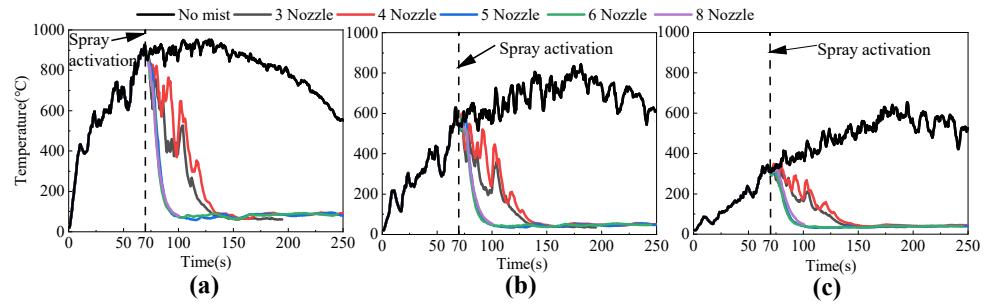


Figure 24. The temperature profiles above the fuel pan: (a) T₁₉; (b) T₂₂; (c) T₂₅.

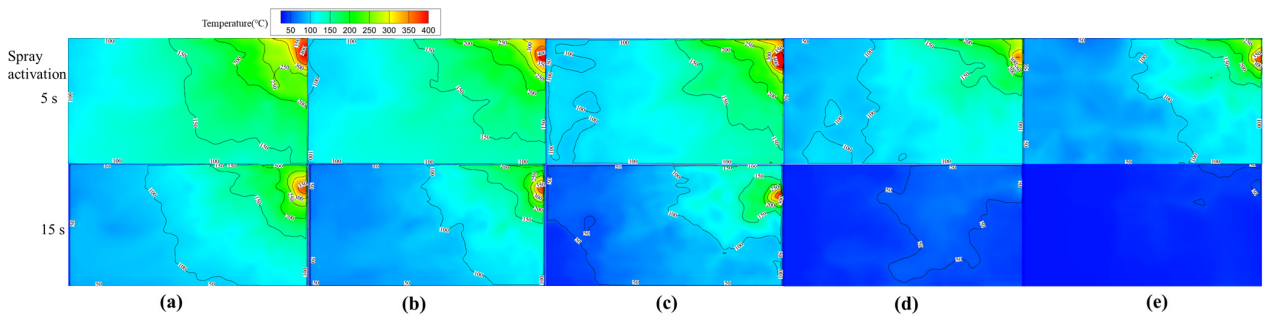


Figure 25. Temperature distribution of a cargo compartment ceiling at 5 s and 15 s after spray activation with different nozzle layouts: (a) 3; (b) 4; (c) 5; (d) 6; (e) 8.

3.4.4. Oxygen Concentration Profiles

The oxygen concentration profiles of the O₁ oxygen sensor for different droplet sizes are shown in Figure 26. The oxygen concentration first decreased quickly due to spray injection until fire extinction and then increased as ambient air entered the container through the ventilation pipe for more than 4 nozzles. In the cases of the 3 and 4 nozzle layouts, the oxygen concentration showed a similar increasing stage after initially decreasing; this could be attributed the fact that due to the relatively small spray coverage area, the fire could not be suppressed quickly, and the interaction between the flame and water mist became more unstable; additionally, the oxygen was introduced again with the air flow induced by the spray dynamic.

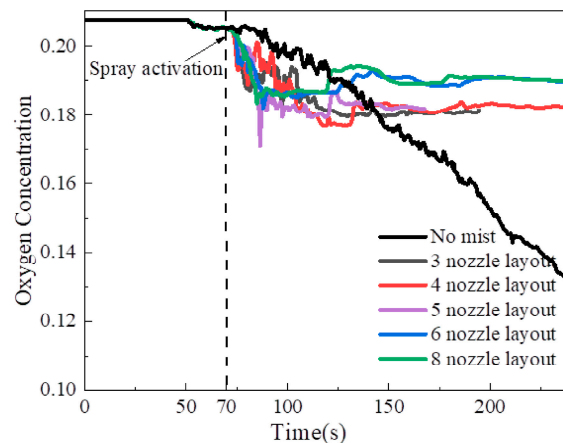


Figure 26. Oxygen concentration results of the O₁ oxygen sensor for different nozzle layouts.

4. Conclusions

In the current study, a series of case studies on the effects of fire location, spray pattern, droplet size, and nozzle layout for fire suppression by water mist in a full-scale

aircraft cargo compartment were conducted using the numerical simulation method. The surface burning fire scenario specified in MPS was selected as the fire source. The influence mechanisms of fire suppression by water mist were revealed via comparisons of HRR, fire extinction time, water consumption, temperature reduction, water mist flux distribution, and oxygen concentration. The findings in this study can be summarized in the following key points:

- (1) Compared with center and sidewall fires, the extinguishment time of the corner fire was relatively larger due to the greater distance from the nozzle, meaning that the effective amount of droplets into the flame area was reduced. In addition, the fire suppression performance of a water mist was not only affected by the distance between fire location and nozzle, but also by the injecting angle of spray.
- (2) The spray pattern showed a significant difference in the spray coverage area and led to differences in fire suppression capability. For a solid spray, most droplets were concentrated at the center, resulting in a smaller coverage area, while for a hollow spray, the spray coverage area increased significantly. The largest spray coverage area occurred at spray angles of (30°, 90°) and (45°, 105°), which is essential to extinguish any possible fire in a cargo compartment. In general, the HRR decay rate and the fire extinction time under a solid spray were relatively larger than the values under a hollow spray, where the minimum extinction time was 104.0 s for the former and the maximum extinction time was 72.0 s for the latter.
- (3) The water mist flux distribution including spray coverage area and flux density was greatly affected by the droplet size. With an increase in the average droplet diameter from 50 µm to 400 µm, the spray coverage area increased and the water mist fluxes at the center below nozzle decreased and gradually diffused to the surrounding edge area. The fire extinction time first increased and then decreased, where the fire suppression efficiency in droplet diameter of 200 µm was the worst, i.e., with a 186.5 s extinction time and 139.88 L in water consumption. The suffocation effect was shown to be the dominant extinguishing mechanism in the case of small droplets, while the cooling effect became more dominant in the case of large droplets. A droplet size of 350 µm was found to be an optimal in our simulation scenario.
- (4) With an increase in number of nozzles, the spray coverage area and the effective water mist entering the flame zone also increased, resulting in a decrease for fire extinguishing time and water consumption. The optimal nozzle configuration scheme needs to consider the influence of water consumption and fire extinguishing time. The 6 nozzle-layout was the best for fire suppression performance in our studied cases.

In this study, quantitative assessments were conducted to examine the extinguishment effects of the spray pattern, droplet size, and nozzle layout by a numerical simulation method. Our research could contribute to the future development of fire suppression by water mist system designs in aircraft cargo compartments. However, it should be noted that due to the use of surrogate fuel and the hypotheses and simplifications of the combustion model and the extinction model, the accuracy of calculation results should be further validated and verified through more large-scale experiments in the future. At the same time, the influences of combustible fuel type and environmental pressure on fire suppression performance should also be considered in order to expand the applicability of water mist systems in future studies. In addition, it is suggested that the use of more fire-resistant materials, particularly for wiring, engines, and aircraft interiors, will significantly reduce the risk of in-flight fires.

Author Contributions: Conceptualization, P.Z. and Q.S.; methodology, P.Z., Z.X. and J.Z.; software, Z.X. and P.Z.; validation, P.Z. and Z.X.; formal analysis, P.Z. and J.Z.; investigation, P.Z. and Z.X.; resources, P.Z.; data curation, Z.X. and J.Z.; writing—original draft preparation, P.Z. and Z.X.; writing—review and editing, P.Z., Q.S. and W.C.; visualization, H.A., J.Z. and Z.X.; supervision, P.Z.; project administration, P.Z.; funding acquisition, P.Z. All authors have read and agreed to the published version of the manuscript.

Funding: This research was funded by the National Natural Science Foundation of China, grant number 52202416, U2233208, Opening Fund of the Key Laboratory of Civil Aviation Thermal Disaster Prevention and Emergency, Civil Aviation University of China, grant number RZH2021-KF-02, Opening Fund of Key Laboratory of Civil Aviation Emergency Science & Technology (CAAC), Nanjing University of Aeronautics and Astronautics, grant numbers NJ2022022 and NJ2023025, the Outstanding Postdoctoral Program of Jiangsu Province.

Institutional Review Board Statement: Not applicable.

Informed Consent Statement: Not applicable.

Data Availability Statement: The data in this study are available from the corresponding author upon reasonable request.

Conflicts of Interest: The authors declare no conflict of interest.

References

1. Wang, J.; Tao, Z.X.; Yang, R.; Gao, Z.S.; Ding, S.; Wang, W. A review of aircraft fire accident investigation techniques: Research, process, and cases. *Eng. Fail. Anal.* **2023**, *153*, 107558. [\[CrossRef\]](#)
2. Speitel, L.C.; Lyon, R.E. *Guidelines for Safe Use of Gaseous Halocarbon Extinguishing Agents in Aircraft*; FAA Report, No. DOT/FAA/AR-08/3; National Technical Information Service (NTIS): Alexandria, VA, USA, 2009.
3. Gann, R.G. Next-generation fire suppression technology program. *Fire Technol.* **1998**, *34*, 363–371. [\[CrossRef\]](#)
4. European Aviation Safety Agency. *Update of CSs in Order to Comply with EC Regulations*; Not. Prop. Amend. (NPA) No. 2011-14; European Aviation Safety Agency: Cologne, Germany, 2011.
5. Tapscott, R.E.; Speitel, L.C. *Options to the Use of Halons for Aircraft Fire Suppression Systems—2012 Update*; FAA Report No. DOT/FAA/AR-11/31; National Technical Information Service (NTIS): Alexandria, VA, USA, 2012.
6. Reinhardt, J.W. *Minimum Performance Standard for Aircraft Cargo Compartment Halon Replacement Fire Suppression Systems (2012 Update)*; FAA Report No. DOT/FAA/TC-TN12/11; National Technical Information Service (NTIS): Alexandria, VA, USA, 2012.
7. Grant, G.; Brenton, J.; Drysdale, D. Fire suppression by water sprays. *Prog. Energy Combust.* **2000**, *26*, 79–130. [\[CrossRef\]](#)
8. Mawhinney, J.R.; Back, G.G. Water mist fire suppression systems. In *SFPE Handbook of Fire Protection Engineering*, 2nd ed.; Springer: Berlin/Heidelberg, Germany, 2016; pp. 1587–1645.
9. Moinuddin, K.; Mahmud, H.M.I.; Joseph, P.; Gamble, G.; Suendermann, B.; Wilkinson, C.; Bossard, J. Experimental and Numerical Studies on the Efficacy of Water Mist to Suppress Hydrocarbon Fires in Enclosures. *Fire* **2024**, *7*, 83. [\[CrossRef\]](#)
10. Liu, Y.S.; Jiang, Z.; Wang, D.; Li, X.H. Experimental research on the water mist fire suppression performance in an enclosed space by changing the characteristics of nozzles. *Exp. Therm. Fluid Sci.* **2014**, *52*, 174–181.
11. Shrigondekar, H.; Chowdhury, A.; Prabhu, S.V. Characterization of a simplex water mist nozzle and its performance in extinguishing liquid pool fire. *Exp. Therm. Fluid Sci.* **2018**, *93*, 441–455. [\[CrossRef\]](#)
12. Kraus-Namrozy, N.; Brzezińska, D. Effectiveness of swirl water mist nozzles for fire suppression. *Int. J. Environ. Res. Public Health* **2022**, *19*, 16328. [\[CrossRef\]](#)
13. Liu, Y.; Fu, Z.X.; Zheng, G.H.; Chen, P. Study on the effect of mist flux on water mist fire extinguishing. *Fire Saf. J.* **2022**, *130*, 103601. [\[CrossRef\]](#)
14. Liu, Y.; Wang, X.; Liu, T.; Ma, J.; Li, G.; Zhao, Z. Preliminary study on extinguishing shielded fire with water mist. *Process Saf. Environ.* **2020**, *141*, 344–354. [\[CrossRef\]](#)
15. Chen, Y.H.; Fang, J.; Zhang, X.L.; Miao, Y.L.; Lin, Y.J.; Tu, R.; Hu, L.H. Pool fire dynamics: Principles, models and recent advances. *Prog. Energy Combust.* **2023**, *95*, 101070. [\[CrossRef\]](#)
16. Baglatzis, M.; Vasilopoulos, K.; Lekakis, I.; Sarris, I. Numerical dimulation of an isolated n-Heptane pool fire. *Fire* **2024**, *7*, 398. [\[CrossRef\]](#)
17. Cavazzuti, M.; Tartarini, P. Pool Fires Within a Large Under-Ventilated Environment: Experimental Analysis and Numerical Simulation Using OpenFOAM. *Fire Technol.* **2024**, *60*, 1891–1915. [\[CrossRef\]](#)
18. Alekseev, V.A.; Soloviova-Sokolova, J.V.; Matveev, S.S.; Chechet, I.V.; Matveev, S.G.; Konnov, A.A. Laminar burning velocities of n-decane and binary kerosene surrogate mixture. *Fuel* **2017**, *187*, 429–434. [\[CrossRef\]](#)
19. Yan, Y.W.; Liu, Y.C.; Fang, W.; Liu, Y.P.; Li, J.H. A simplified chemical reaction mechanism for two-component RP-3 kerosene surrogate fuel and its verification. *Fuel* **2018**, *227*, 127–134. [\[CrossRef\]](#)
20. Humer, S.; Frassoldati, A.; Granata, S.; Faravelli, T.; Ranzi, E.; Seiser, R.; Seshadri, K. Experimental and kinetic modeling study of combustion of JP-8, its surrogates and reference components in laminar nonpremixed flows. *Proc. Combust. Inst.* **2007**, *31*, 393–400. [\[CrossRef\]](#)
21. Pio, G.; Carboni, M.; Salzano, E. Realistic aviation fuel chemistry in computational fluid dynamics. *Fuel* **2019**, *254*, 115676. [\[CrossRef\]](#)
22. Zhu, P.; Wang, X.; Wang, Z.; Cong, H.; Ni, X. Experimental and numerical study on attenuation of thermal radiation from large-scale pool fires by water mist curtain. *J. Fire Sci.* **2015**, *33*, 269–289. [\[CrossRef\]](#)

23. Jenft, A.; Collin, A.; Boulet, P.; Pianet, G.; Breton, A.; Muller, A. Experimental and numerical study of pool fire suppression using water mist. *Fire Saf. J.* **2014**, *67*, 1–12. [[CrossRef](#)]
24. Beji, T.; Ebrahim Zadeh, S.; Maragkos, G.; Merci, B. Influence of the Particle Injection Rate, Droplet Size Distribution and Volume Flux Angular Distribution on the Results and Computational Time of Water Spray CFD Simulations. *Fire Saf. J.* **2017**, *91*, 586–595. [[CrossRef](#)]
25. Liu, H.R.; Wang, C.; De Cachinho Cordeiro, I.M.; Yuen, A.C.Y.; Chen, Q.; Chan, Q.N.; Kook, S.; Yeoh, G.H. Critical Assessment on Operating Water Droplet Sizes for Fire Sprinkler and Water Mist Systems. *J. Build Eng.* **2020**, *28*, 100999. [[CrossRef](#)]
26. Lee, J. Numerical Analysis of How Ventilation Conditions Impact Compartment Fire Suppression by Water Mist. *Ann. Nucl. Energy* **2020**, *136*, 107021. [[CrossRef](#)]
27. Dasgotra, A.; Rangarajan, G.; Tauseef, S.M. CFD-based study and analysis on the effectiveness of water mist in interacting pool fire suppression. *Process Saf. Environ.* **2021**, *152*, 614–629. [[CrossRef](#)]
28. Ha, G.; Shin, W.G.; Lee, J. Numerical Analysis to Determine Fire Suppression Time for Multiple Water Mist Nozzles in a Large Fire Test Compartment. *Nucl. Eng. Technol.* **2021**, *53*, 1157–1166. [[CrossRef](#)]
29. Robinet, A.; Chetehouna, K.; Cablé, A.; Florentin, É.; Oger, A. Numerical Investigations on Water Mist Fire Extinguishing Performance: Physical and Sensitivity Analysis. *Fire* **2022**, *5*, 176. [[CrossRef](#)]
30. Cordeiro, I.M.D.C.; Liu, H.; Yuen, A.C.Y.; Chen, T.B.Y.; Li, A.; Wang, C.; Cao, R.; Yeoh, G.H. On the Large Eddy Simulation Modelling of Water Suppression Systems Droplet Impact and Coverage Area. *Fire* **2022**, *5*, 165. [[CrossRef](#)]
31. Gui, X.H.; Xue, H.T.; Hu, Z.Y.; Cui, Z.H. Influence of Water Mist Nozzle Characteristic Parameters on Oil Pool Fire Extinguishing in Confined Space. *Arab. J. Sci. Eng.* **2023**, *48*, 3441–3454. [[CrossRef](#)]
32. Vilfayeau, S.; Myers, T.; Marshall, A.W.; Trouvé, A. Large eddy simulation of suppression of turbulent line fires by base-injected water mist. *Proc. Combust. Inst.* **2017**, *36*, 3287–3295. [[CrossRef](#)]
33. Liu, H.R.; Yuen, A.C.Y.; Cordeiro, I.M.D.C.; Han, Y.; Chen, T.B.Y.; Chan, Q.N.; Kook, S.; Yeoh, G.H. A novel stochastic approach to study water droplet/flame interaction of water mist systems. *Numer. Heat Trans.-Appl.* **2021**, *79*, 570–593. [[CrossRef](#)]
34. Dinesha, A.; Benson, C.M.; Holborn, P.G.; Sampath, S.; Xiong, Y. Performance Evaluation of Nitrogen for Fire Safety Application in Aircraft. *Reliab. Eng. Syst. Safe.* **2020**, *202*, 107044. [[CrossRef](#)]
35. Marker, T.R.; Reinhardt, J.W. *Water Spray as a Fire Suppression Agent for Aircraft Cargo Compartment Fires*; FAA Report, No. DOT/FAA/AR-TN01/1; National Technical Information Service (NTIS): Alexandria, VA, USA, 2001.
36. Reinhardt, J.W. *The Evaluation of Water Mist with and Without Nitrogen as an Aircraft Cargo Compartment Fire Suppression System*; FAA Report No. DOT/FAA/AR-01/121; National Technical Information Service (NTIS): Alexandria, VA, USA, 2002.
37. Payri, R.; Gimeno, J.; Martí-Aldaraví, P.; Carvallo, C. Parametrical Study of the Dispersion of an Alternative Fire Suppression Agent Through a Real-Size Extinguisher System Nozzle Under Realistic Aircraft Cargo Cabin Conditions. *Process Saf. Environ.* **2020**, *141*, 110–122. [[CrossRef](#)]
38. Xiong, Y.F.; Diakostefanis, M.; Dinesh, A.; Sampath, S.; Nikolaidis, T. Numerical Assessment for Aircraft Cargo Compartment Fire Suppression System Safety. *J. Fire Sci.* **2021**, *39*, 240–261. [[CrossRef](#)]
39. Pathak, A.; Norrefeldt, V.; Pschirer, M. Validation of a Simulation Tool for an Environmentally Friendly Aircraft Cargo Fire Protection System. *Aerospace* **2021**, *8*, 35. [[CrossRef](#)]
40. Zhu, P.; Luo, S.F.; Liu, Q.Y.; Shao, Q.; Yang, R. Effectiveness of Aviation Kerosene Pool Fire Suppression by Water Mist in a Cargo Compartment with Low-Pressure Environment. *J. Tsinghua Univ. (Sci. Technol.)* **2022**, *62*, 21–32.
41. Huang, S.P.; Zhu, P.; Liu, Q.Y.; Shao, Q. Numerical Simulation Study on Synergetic Fire Suppression of Nitrogen/Water-Mist in Cargo Compartment. *J. Beijing Univ. Aeronaut. Astronaut.* **2022**, 1–14. [[CrossRef](#)]
42. McGrattan, K.; Hostikka, S.; McDermott, R.; Floyd, J.; Weinschenk, C.; Overcompartment, K. *Fire Dynamics Simulator User's Guide (FDS)*, 6th ed.; National Institute of Standards and Technology: Gaithersburg, MD, USA, 2020.
43. McGrattan, K.; Hostikka, S.; Floyd, J.; McDermott, R.; Vanella, M. *Fire Dynamics Simulator Technical Reference Guide Volume 1: Mathematical Model*; National Institute of Standards and Technology: Gaithersburg, MD, USA, 2020.
44. Babrauskas, V. Chapter 26: Heat release rate. In *SFPE Handbook of Fire Protection Engineering*, 5th ed.; Springer: New York, NY, USA, 2016; pp. 799–904.
45. Yu, H.Z.; Lee, J.L.; Kung, H.C. Suppression of Rack-Storage Fires by Water. *Fire Saf. Sci.* **1994**, *4*, 901–912. [[CrossRef](#)]
46. Hamins, A.; McGrattan, K.B. *Reduced-Scale Experiments to Characterize the Suppression of Rack-Storage Commodity Fires*; NIST Tech. Rep. NISTIR 6439; National Institute of Standards and Technology: Gaithersburg, MD, USA, 1999.

Disclaimer/Publisher's Note: The statements, opinions and data contained in all publications are solely those of the individual author(s) and contributor(s) and not of MDPI and/or the editor(s). MDPI and/or the editor(s) disclaim responsibility for any injury to people or property resulting from any ideas, methods, instructions or products referred to in the content.